

Development of an enhanced hybrid piecewise logistic model for retrieving land surface phenology in drylands

Yongchang Ye^a, Xiaoyang Zhang^{a,*}, Jianmin Wang^b, Khuong H. Tran^{a,c,d}, Yuxia Liu^a, Yu Shen^a, Shuai Gao^a, Shuai An^a

^a Geospatial Sciences Center of Excellence, Department of Geography and Geospatial Sciences, South Dakota State University, Brookings, SD 57007, USA

^b Department of Forestry and Natural Resources, Purdue University, West Lafayette, IN 47907, USA

^c NASA Ames Research Center, Moffett Field, CA 94035, USA

^d Bay Area Environmental Research Institute, Moffett Field, CA 94035, USA

ARTICLE INFO

Edited by Marie Weiss

Keywords:

LSP
Drylands
Plateau stages
Irregular time series
Logistic model
VIIRS
PhenoCam

ABSTRACT

The accurate retrieval of land surface phenology (LSP) for drylands is extremely challenging. Drylands exhibit vegetation characteristics such as sparse and patchy vegetation cover, low seasonal greenness variability, and high spatial heterogeneity. The irregular rainy and dry episodes often complicate vegetation growth, leading to an irregular temporal trajectory with multiple growth stages during the greenup and senescence phases. Moreover, the heterogeneous phenological cycles among the vegetation species in a satellite pixel and other factors may lead to a long period with only a very slight increase or decrease in greenness before or after a vegetation growing cycle. Current phenological retrieval methods, however, commonly assume that vegetation greenness gradually increases in a greenup phase and decreases in a senescence phase, following a single sigmoidal growth trajectory, which is inadequate to describe the irregular growth in drylands. In this study, we developed a novel algorithm to improve on the hybrid piecewise logistic model (HPLM) for improving LSP retrievals, especially in drylands. Our enhanced HPLM (E-HPLM) algorithm addresses two characteristics of irregular growth trajectories: (1) the multiple plateau stages within a greenup or senescence phase, and (2) the long linear tail before the start or after the end of a growing season. Specifically, we identified multiple growth stages within a greenup or senescence phase in order to fit each stage separately with a logistic model, and added a linear parameter to the logistic model to eliminate long linear tails by adjusting the background values. We implemented this new algorithm to retrieve LSPs in global drylands using the 500 m Visible Infrared Imaging Radiometer Suite (VIIRS) dataset from 2013 to 2022. The results were then compared with those of HPLM-retrieved LSPs. We also evaluated the E-HPLM results using phenometrics derived from the PhenoCam observations at site levels and the fused Harmonized Landsat and Sentinel-2 (HLS)-PhenoCam dataset at regional levels. The E-HPLM was able to reduce the uncertainty by ~10 days in the pixels with plateau stages from 2013 to 2022 in global drylands in comparison with the HPLM algorithm, where the plateau stage appeared in over 74 % of drylands. Compared with the HPLM, the E-HPLM improved overall phenology accuracy by two days for the PhenoCam sites and one to four days in HLS-PhenoCam areas, although the improvements varied with land cover types and aridity levels. The E-HPLM algorithm has the potential to replace the current HPLM algorithm, with improved ability to retrieve LSP in drylands and to generate global LSP products.

1. Introduction

Drylands cover roughly 40 % of the land surface, produce about 44 % of crops, and contain over 30 % of the world's population and a diverse range of human cultures (UNCCD, 2017). Global drylands are distributed over a variety of climatic zones, and are characterized by low

precipitation and high evaporation (Middleton and Sternberg, 2013). Due to strong water constraints, dryland ecosystems are vulnerable to climate variability (Lian et al., 2021) and human activities (Wang et al., 2023). Although vegetation density and annual productivity are low in drylands, these areas play an important role in regulating the trend and interannual variability of the global carbon dioxide sink (Ahlström et al.,

* Corresponding author.

E-mail address: xiaoyang.zhang@sdstate.edu (X. Zhang).

2015). Thus, changes in dryland phenological metrics could significantly alter the exchange of carbon dioxide between the atmosphere and biosphere (Richardson et al., 2013).

The vegetation phenology in drylands shows strong responses to precipitation, an effect that has been well demonstrated in various arid and semiarid regions. For example, the start and end of the vegetation growing seasons were respectively triggered by the start and end of the rainy seasons in Africa, with strong local shifts (Zhang et al., 2005). The phenology pattern across a savanna transect in north Australia was found to closely follow the rainfall pulse (Ma et al., 2013). Rainfall pulses characterized by high frequency and low intensity favor shallow-rooted vegetation species with quick responses (Cook et al., 2002). The spring phenology in the Tibetan Plateau shows stronger preseason precipitation impacts in drier than in wetter areas, while the impacts of preseason temperature are stronger in wetter than drier areas (Shen et al., 2015). Furthermore, the preseason precipitation may have impacts on the long period of the growing season, and extreme drought events can increase the sensitivity of vegetation to rainfalls (Xie and Lark, 2021). Seasonal vegetation variability is complex, although annual precipitation may explain the spatial gradients of greenness in dryland vegetation (Ukkola et al., 2021; Zhang et al., 2022). Moreover, drought stress can shorten the growing season for grass by either delaying the greenup date or advancing the senescence date according to a long-term control experiment in a semiarid grassland (Currier and Sala, 2022). The resilience of vegetation to drought varies largely among different plant species. For example, C₄ species have stronger drought tolerance than C₃ species, but C₃ plant abundance can increase explosively under low rainfall (in cooler months) in years with extreme drought (Knapp et al., 2020).

Land surface phenology (LSP) can be accurately retrieved from satellite data for forests and croplands in temperate and continental climates across the globe (Hmimina et al., 2013; Piao et al., 2006; Zhang et al., 2004). In these regions, and particularly at mid-high latitudes, vegetation growth follows a regular temporal pattern involving a vegetation growth cycle where the vegetation index (VI) continuously increases during the greenup phase, reaches a relatively stable period of maximum leaf area, sustainably decreases during the senescence phase, and reaches a minimum during the dormant phase (Zhang et al., 2003). However, currently available algorithms have performed less effectively in drylands (Liu et al., 2017c; Peng et al., 2021; Xie et al., 2022; Zhang et al., 2020), and the phenological metrics (phenometrics) retrieved for drylands have always shown a much larger bias than those for other climates and ecosystems (Peng et al., 2017b; Richardson et al., 2018; Ye et al., 2022; Zhang et al., 2018a). This issue is closely linked to the unique characteristics of drylands, such as: (1) sparse vegetation cover and high background noise; (2) patchy and heterogeneous spatial distributions of vegetation; and (3) sporadic precipitation episodes and frequent periods of drought (Smith et al., 2019). Due to these characteristics, the commonly used VI time series, such as the normalized difference vegetation index (NDVI), the Enhanced vegetation index (EVI), and two-band EVI (EVI2), may show subtle variations in greenness and irregular temporal trajectories.

In contrast to the regular temporal pattern of vegetation growth (Zhang et al., 2003), the VI time series in drylands often exhibits two characteristics: (1) multiple plateau stages in the middle of the greenup and senescence phases, and (2) long linear tails during the early greenup period or the late senescence period, which are referred to here as irregular trajectories or variations. These two characteristics have been clearly shown in previous studies, such as the Moderate Resolution Imaging Spectroradiometer (MODIS) EVI curve in northwestern China (Cao et al., 2015), the MODIS and Visible Infrared Imaging Radiometer Suite (VIIRS) NDVI curve for the oak and grass savanna of California (Liu et al., 2017c), the Harmonized Landsat-8 Sentinel-2 (HLS) NDVI curve in the western U.S. (Pastick et al., 2018), the OCO-2 solar-induced chlorophyll fluorescence (SIF) curve in Australia (Wang et al., 2019), and the PlanetScope EVI2 curve in the United States (Liu et al., 2024; Moon

et al., 2021; Moon et al., 2022). The plateau stage is mainly forced by drought events and heterogeneous plant species (Liu et al., 2017c). In addition, the plateau stages may be potentially associated with data processes in the period with persistent cloud contamination (such as the Bidirectional Reflectance Distribution Function (BRDF) model established using a 16-day moving window for data filling) in the VIIRS product (Schaaf et al., 2018). A slight increase in greenness before the greenup phase of the vegetation community is likely to be associated with the variation in rare species, insufficient water to support regular vegetation growth (Liu et al., 2017c), or residual snow impacts (Delbart et al., 2005), while a slight decrease in greenness after the senescence phase could be associated with the plants drying out slowly after the end of the growing season.

LSP retrievals for drylands remain challenging, although various algorithms have been developed, including Fourier transformations (Moody and Johnson, 2001), asymmetric Gaussian functions (Jonsson and Eklundh, 2002), logistic functions (Zhang et al., 2003), polynomial functions (Piao et al., 2006), and cubic splines (Hmimina et al., 2013). A few approaches have been proposed for modeling irregular VI trajectories. The first of these involves modification of the logistic function by adding a plant stress parameter or “brown down” parameter (Elmore et al., 2012); this works well in terms of describing the VI variation in the maturity phase (around peak VI) in forests (Zhang, 2015), but cannot be applied to the plateau stage during the middle of the periods of VI increase or decrease. The second approach uses a non-parametric fitting function, such as the cubic spline method (Hmimina et al., 2013). However, the cubic spline is very sensitive to uncertainties in the VI time series, which are frequent in satellite observations, and some changes in the modeled curve lack biological meanings, especially in evergreen forests (Hmimina et al., 2013). The third approach only models the part of the curvature where the shape matches the logistic function (Cao et al., 2015), and is unable to generate temporal trajectories for an entire growing season. The fourth approach simply relates the phenometrics to a threshold for the amplitude of vegetation growth after smoothing with a window size of four months, and ignores irregular patterns in VI time series or vegetation growth (Xie et al., 2022).

In view of the challenges associated with appropriately fitting irregular VI trajectories, phenometrics in drylands are frequently unretrieved or retrieved with large uncertainties from currently available LSP products (Peng et al., 2017b), including the most recent NASA 500 m land cover dynamics product (MCD12Q2 C6) from MODIS data (Gray et al., 2019), the 500 m global LSP product (VNP22Q2 V001) from VIIRS (Zhang et al., 2018b), and 30 m LSP product from HLS data (Bolton et al., 2020). In addition, the phenology derived from SIF data shows a very large bias, which arises from the complex mixture of species and irregular rainfall events (Wang et al., 2019).

In this study, we refine the logistic model to reconstruct the irregular VI trajectories, in order to address the issues of multiple plateau stages and long linear tails. We hypothesized that a greenup or senescence phase containing plateau stages arises from the integration of multiple pieces of short-period logistic growth curves; in other words, an irregular VI trajectory is composed of a set of regular short VI trajectories. We further hypothesize that the linear tail represents the slow variations before or after the actual seasonal vegetation growth in a satellite pixel, and that this can be eliminated by adding a linear parameter to tune the background value in the logistic function. Based on these two hypotheses, we enhanced the logistic model to fit irregular VI trajectories. The algorithm is tested on LSP retrievals in global drylands from 2013 to 2022 and is evaluated using PhenoCam observations as well as a fusion of HLS and PhenoCam observations. The new model proposed in this paper shows a promise in effectively reconstructing high-quality VI time series with irregular patterns and to generate a global LSP product with high accuracy for drylands.

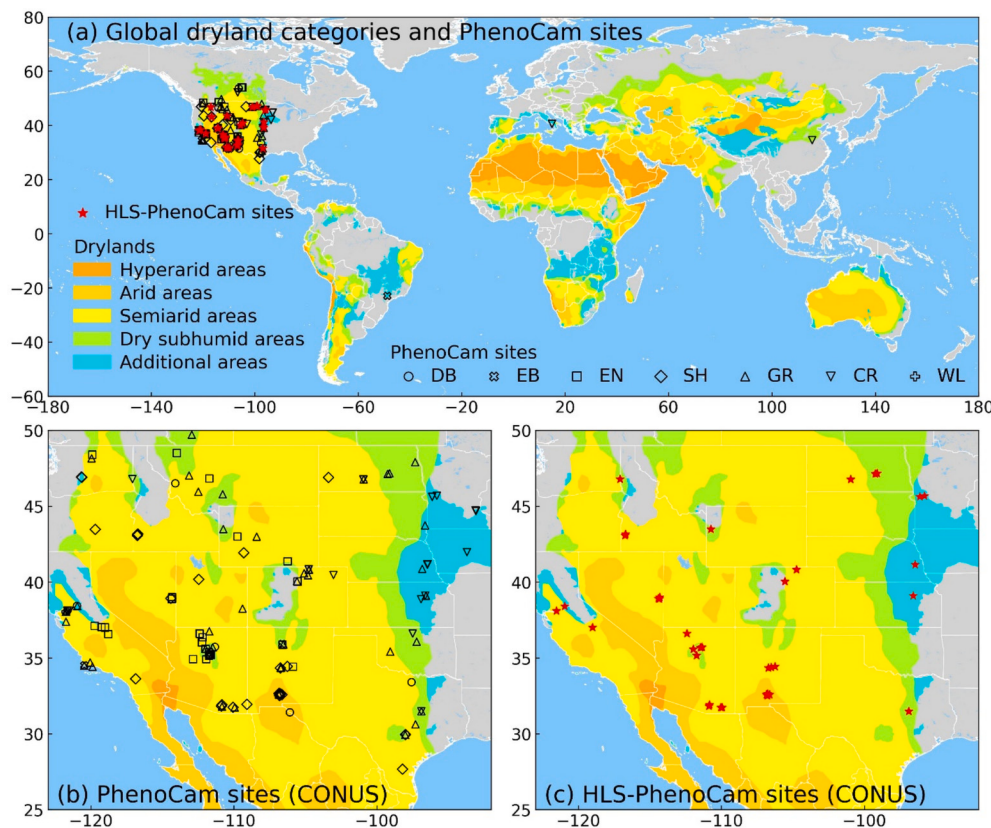


Fig. 1. Spatial distribution of dryland categories, HLS-PhenoCam sites, and PhenoCam sites in global drylands. (a) Global dryland categories and PhenoCam sites with different land cover types; (b) PhenoCam sites with different land cover types in the western CONUS; (c) HLS-PhenoCam regions in the western CONUS. CONUS: continental United States, DB: deciduous broadleaf, EB: evergreen broadleaf, EN: evergreen needleleaf, SH: shrublands, GR: grasslands, CR: croplands, WL: wetlands.

Table 1
Dryland categories and proportion (%) of drylands in the global land.

Drylands	Aridity index	North America	Europe	Asia	South America	Africa	Australia	Average
Hyper-arid areas	< 0.05	0.1	0.0	4.6	1.4	23.4	0.0	5.0
Arid areas	0.05–0.20	2.3	0.3	12.0	2.7	17.0	39.2	12.2
Semi-arid areas	0.20–0.50	11.6	8.3	14.5	15.1	17.0	39.9	17.7
Dry sub-humid areas	0.50–0.65	7.7	17.3	7.4	11.8	9.2	7.7	10.2
Additional areas	≥ 0.65	1.3	3.3	4.9	16.5	12.8	5.4	7.4
Total		23.0	29.2	43.4	47.5	79.4	92.2	52.5

2. Materials

2.1. Global drylands

The global dryland boundary shapefile was downloaded from the United Nations Environment Programme - World Conservation Monitoring Centre (<https://resources.unep-wcmc.org/>) (Fig. 1a). This was originally developed to define the boundaries of drylands as part of the Millennium Ecosystem Assessment received from the National Biological Information Infrastructure project at the United States Geological Survey (Millennium Ecosystem Assessment, 2005). For this boundary dataset, the definition of drylands was adopted from the United Nations Convention to Combat Desertification (UNCCD). Based on the aridity index (AI), which is calculated by dividing the potential evapotranspiration by the annual average precipitation, the drylands (AI < 0.65) were classified into four categories (UNCCD, 1994, 2017): hyper-arid areas, arid areas, semi-arid areas, and dry sub-humid areas. To better reflect the biological diversity of dry and sub-humid lands, the Convention on Biological Diversity (CBD) provides a broader and less precise definition of drylands by including a category of additional areas with AI values

above 0.65 but also showing dryland features (UNEP/CBD/SBSTTA/5, 1999). The dataset used in this study consisted of five categories that were constructed by incorporating both the UNCCD and CBD definitions of drylands (Sorensen, 2007). Thus, the total dryland areas in the five categories are found in over 50 % of the global land (Table 1).

2.2. VIIRS nadir-BRDF-adjusted reflectance (NBAR) and land surface temperature data

The VIIRS BRDF-Adjusted Reflectance (NBAR) product (VNP43IA4) was acquired as the primary input for LSP retrievals. The daily NBAR product is created using the RossThick/Li-Sparse-Reciprocal (RTLSR) semi-empirical kernel-driven BRDF model (Schaaf et al., 2018). The RTLSR model is established based on a moving window of 16-day VIIRS observations, and is used to reconstruct the surface anisotropic effects and correct the view angle to the nadir and the solar zenith angle to local solar noon. This NBAR product is produced daily with a spatial resolution of 500 m, in three imagery bands (I1: red, I2: near-infrared (NIR), and I3: short-wave infrared) and their associated quality flags (0: NBAR retrieval from the full inversion model; 1: NBAR retrieval from the

backup magnitude inversion model; and 255: no surface retrievals due to cloud cover or a lack of VIIRS observations). To determine the NBAR when contaminated with snow cover, the snow flag indicating the occurrence of snow was obtained from the VIIRS BRDF/Albedo Quality product (VNP43IA2). In this study, the daily EVI2 was calculated from the red and NIR bands. An EVI2 result was assigned as high quality if the quality flags for the red and NIR bands were both zero, and as low quality if either of the quality flags in the two bands was one. Furthermore, the fill value was assigned to the dates with snow cover and without valid NBAR.

The VIIRS daily land surface temperature (LST) product (VNP21A1D) was also obtained as ancillary data for LSP retrievals (Hulley et al., 2016). The 1 km LST data were resampled to 500 m using a nearest neighbor method to match the spatial resolution of VIIRS EVI2, and the LST value was used to determine the duration of the winter period (Zhang, 2015).

These VIIRS products from 2013 to 2022 were downloaded from the NASA Land Processes Distributed Active Archive Center (LP DAAC) (<https://ladsweb.modaps.eosdis.nasa.gov/>).

2.3. VIIRS global land surface phenology (GLSP) product

The VIIRS GLSP product (VNP22Q2) provides global LSP metrics with a 500 m spatial resolution on a yearly basis (Zhang, 2024), and is available from NASA LP DAAC. It is derived from the time series of EVI2 calculated from VIIRS NBAR. This product contains six phenological transition dates: onset of greenness increase (greenup onset), onset of greenness maximum (maturity onset), onset of greenness decrease (senescence onset), onset of greenness minimum (dormancy onset), date of mid-greenup phase, and date of mid-senescence phases. It also includes greenness-related metrics and quality control layers. All the data layers are identified for up to two growing cycles per year. The algorithm used to generate the VIIRS GLSP product is the hybrid piecewise logistic model (HPLM) (Zhang, 2015; Zhang et al., 2018b). In this study, four key phenological transition dates (greenup onset, maturity onset, senescence onset, and dormancy onset) and the length of the growing season from 2013 to 2022 were extracted from the VIIRS GLSP product, which was taken as a reference (hereafter termed VIIRS HPLM).

2.4. MODIS land cover product

The MODIS land cover type product (MCD12Q1, yearly, 500 m) for 2013–2022 was also downloaded from NASA LP DAAC (Sulla-Menashe et al., 2019). This product provides land cover types based on the International Geosphere-Biosphere Programme (IGBP), University of Maryland (UMD), Leaf Area Index (LAI), BIOME-Biogeochemical Cycles (BGC), and Plant Functional Types (PFT) classification schemes (Friedl and Sulla-Menashe, 2022). In this case, the IGBP classification was extracted for the phenological retrieval algorithm to identify whether multiple growing cycles existed in a calendar year based on the assumption that some land cover types cannot have multiple vegetation growing cycles within a year period (Section 3.1), and it was also used to assess the retrieved LSP for different land cover types (Section 3.3).

2.5. PhenoCam observations

The PhenoCam dataset for 2013–2022 was downloaded from the PhenoCam website (<https://phenocam.nau.edu/webcam/>). It consists of red, green, and blue (RGB) images in JPEG format with an observation frequency of ~30 min. Although PhenoCam imagery does not directly match the spatial and geometric characteristics of satellite observations, it is still one of the best datasets for satellite LSP validation, because it provides cloud-free and human eye-discernible visualization.

To derive the phenometrics from the PhenoCam images, we carried out the following steps. (1) The region of interest (ROI) for each site was defined using the xROI tool (<https://github.com/bnasm/xROI>). Since the

Table 2

Numbers of PhenoCam sites/site-years in different dryland categories and land cover types. DB: deciduous broadleaf, EB: evergreen broadleaf, EN: evergreen needleleaf, SH: shrublands, GR: grasslands, CR: croplands, WL: wetlands, -: does not exist.

Drylands	DB	EB	EN	SH	GR	CR	WL	Total
Hyper-arid areas	–	–	–	–	–	–	–	–
Arid areas	–	–	–	5/ 20	3/6	–	–	8/26
Semi-arid areas	5/ 12	–	20/ 49	11/ 33	19/ 43	9/ 22	4/ 4	68/ 163
Dry sub-humid areas	1/1	2/ 3	7/ 11	–	21/ 38	4/9	–	35/62
Additional areas	1/6	1/ 3	–	1	4/ 11	14/ 22	–	21/41
Total	7/ 19	3/ 6	27/ 60	17/ 54	47/ 98	27/ 53	4/ 4	132/ 294

field of view (FOV) of a PhenoCam image is usually smaller than a 500 m VIIRS pixel, a ROI was selected by covering the largest possible vegetated area, to give a good spatial match between the VIIRS pixel and the corresponding PhenoCam observation. (2) Each band in the ROI of an RGB image was averaged to get the digital numbers DN_{red} , DN_{green} , and DN_{blue} . (3) The green chromatic coordinate (GCC) for each image was calculated by dividing the sum of DN_{red} , DN_{green} , and DN_{blue} by DN_{green} (Klosterman et al., 2014). (4) The half-hourly GCC time series was composited into a 3-day series by calculating the 90th percentile of all the GCC values within three days. (5) The 3-day GCC time series was used for LSP retrievals using the HPLM algorithm.

To examine the differences between the HPLM and E-HPLM, we selected sites based on six criteria: (1) located in drylands, (2) in the view of vegetation canopy, (3) a roughly spatial match with a VIIRS pixel based on visualization, (4) missing observations of less than 90 days in a full year, (5) an EVI2 time series for the corresponding VIIRS pixels with either plateau stages or linear tails (note that the HPLM and E-HPLM produced same retrievals for regular time series), and (6) a phenological difference between the PhenoCam observations and VIIRS GLSP product of less than 90 days. We note that the PhenoCam and VIIRS temporal profiles were not comparable if the difference in phenological dates was larger than 90 days. The temporal mismatch was mainly caused by the mismatch of observed spatial coverages. Finally, 132 sites (294 site-years) were selected (Table 2), which were mostly located in the continental United States (CONUS) (Fig. 1a, b).

2.6. 30 m HLS-PhenoCam LSP dataset

The HLS-PhenoCam dataset was produced from the fusion of the HLS and PhenoCam time series (Tran et al., 2023). This dataset is available from the Oak Ridge National Laboratory (ORNL) Distributed Active Archive Center (DAAC) (<https://daac.ornl.gov/>), and provides phenometrics (greenup onset, maturity onset, senescence onset, and dormancy onset) at a spatial resolution of 30 m for 78 10 × 10 km² regions centered at PhenoCam sites in North America from 2019 and 2020. The phenometrics were retrieved using the HPLM algorithm from the associated 3-day gap-free EVI2 time series that were generated by fusing the HLS EVI2 time series with temporal trajectories of PhenoCam GCC. The synthesis of satellite and ground-based PhenoCam observations means that the retrieved phenometrics represent a high-quality reference (hereafter termed HLS-PhenoCam HPLM) for validating other satellite LSP products. This dataset has an advantage over PhenoCam data in that it is scalable to match other moderate or coarse pixels spatially at a regional scale of 100 km². For this study, we obtained 36 HLS-PhenoCam regions in drylands across the CONUS (Fig. 1c).

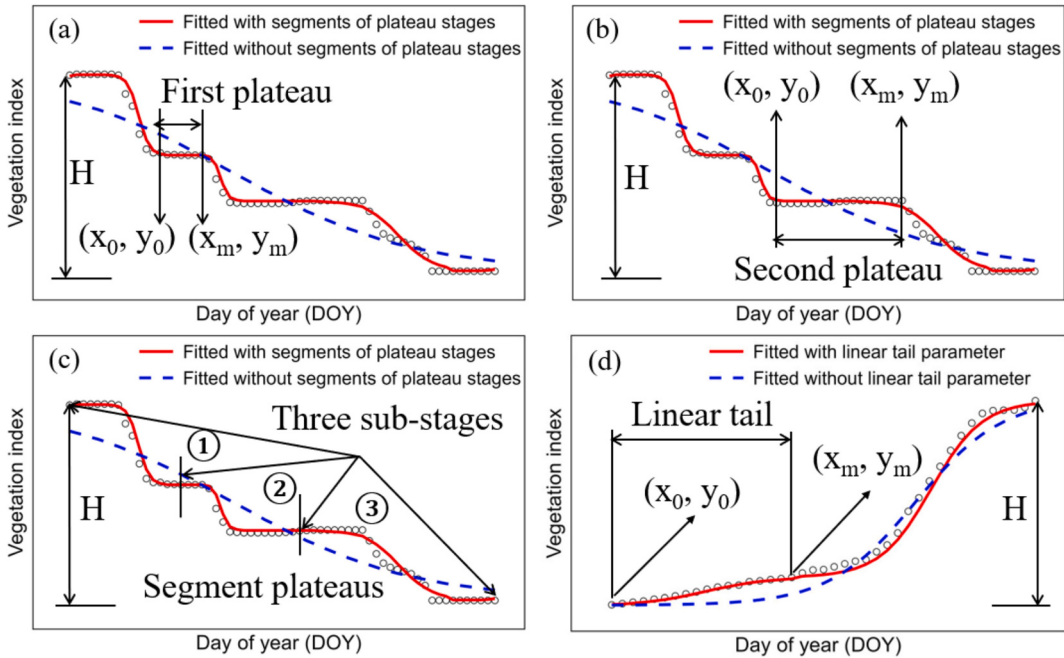


Fig. 2. Illustration of the enhancement algorithm for land surface phenology retrievals. (a) Determining the first plateau in a senescence phase; (b) determining the second plateau in a senescence phase; (c) dividing the senescence phase into three sub-stages (segments) using the mid-points in the two plateaus and then fitting each sub-stage separately; and (d) determining a linear tail in the lower part of a section. H represents the amplitude of a growing cycle. (x_0, y_0) and (x_m, y_m) are the starting and ending points of a plateau stage or a linear tail.

3. Method

3.1. Development of the enhanced hybrid piecewise logistic model (E-HPLM)

The E-HPLM algorithm for phenological retrievals was developed on the basis of the HPLM algorithm.

3.1.1. Hybrid piecewise logistic model (HPLM)

Although HPLM has been well-documented and widely applied in previous studies (Tran et al., 2023; Zhang, 2015; Zhang et al., 2003), the HPLM algorithm is briefly described here, as follows. (1) The daily EVI2 (or other VIs) time series is calculated from the VIIRS NBAR (or other satellite surface reflectance) product, which is used to generate a 3-day EVI2 composite by selecting the maximum of all the best quality EVI2 within three days. The selection of a 3-day period is made because vegetation (such as crop and grass) growth stages are shorter than one week (Ammar and Davies, 2019; Reeves et al., 2001), and a temporal VI composite period of more than six days could significantly increase the uncertainty in phenology retrievals (Zhang et al., 2009) and decrease the capability to trace temporal vegetation dynamics (Kandasamy et al., 2013; Kross et al., 2011; Pouliot et al., 2011). Moreover, the 3-day composite reduces the data volume relative to daily data but retains fine temporal information. (2) A 3-day EVI2 time series for a two-year period, which consists of the preceding half year, the given year, and the succeeding half year, is generated for retrieving phenological dates in the current year. This EVI2 time series enables capture of the vegetation growing cycle, which may span two calendar years. (3) Noise is removed from the 3-day EVI2 time series using a series of smoothing functions, including a moving window smooth method, a moving median method, and Savitzky-Golay filters. Furthermore, the local valleys in the EVI2 time series (pseudo growing cycles) are removed using a moving average of the high-quality values at the neighboring peaks, based on the assumption that there are no two vegetation growing peaks (cycles) within four months for forests and two months for shrublands, grasslands, and croplands. (4) The background EVI2 (minimum EVI2 in

the dormancy period) is determined by calculating the average of the 15 % of the largest EVI2 values with $LST < 5^{\circ}\text{C}$ and 5 % of the smallest EVI2 values with $LST > 5^{\circ}\text{C}$. (5) The EVI2 time series is segmented into multiple segments of greenup and senescence phases using changes from positive to negative slope within a moving window consisting of five EVI2 values, and vice versa. The segment with small amplitude in the EVI2 time series is excluded because it is commonly caused by abiotic factors instead of vegetation growth cycles. The excluded segment is determined by its amplitude being smaller than one-third of the annual amplitude and its maximum EVI2 being smaller than two-thirds of the annual maximum EVI2. This process enables the identification of multiple growth cycles within a 12-month period. (6) Each greenup or senescence phase is fitted with a logistic function (Eq. (1)).

$$\text{EVI2}(t) = \begin{cases} \frac{\text{EVI2}_{\text{amplitude}}}{1 + e^{a+b \times t}} + \text{EVI2}_{\text{background}} & \text{Favorable growth condition} \\ \frac{\text{EVI2}_{\text{amplitude}} + d \times t}{1 + e^{a+b \times t}} + \text{EVI2}_{\text{background}} & \text{Vegetation stress condition} \end{cases} \quad (1)$$

where t is the time in calendar days of year (DOY), a is related to the vegetation growth period, b is associated with the rate of plant leaf development, d is a vegetation stress factor, $\text{EVI2}_{\text{amplitude}}$ is the amplitude of EVI2 variation, and $\text{EVI2}_{\text{background}}$ is the background (minimum) EVI2 value.

Finally, the rate of change in the curvature is calculated along the fitted EVI2 curve in the HPLM, and the extreme points are used to obtain the corresponding phenological transition dates. Greenup onset and maturity onset correspond to the two largest extreme points during a greenup phase, respectively, while senescence onset and dormancy onset correspond to the two smallest extreme points during a senescence phase, respectively. In a biophysical sense, these onsets reflect the following vegetation phenological dates: greenup onset (leaf-out), or the date on which greenness starts increasing (i.e. start of growing season, SOS); maturity onset, or the date on which greenness reaches a maximum; senescence onset, or the date on which greenness starts decreasing; and dormancy onset or the date on which greenness reaches

a minimum (i.e. end of growing season, EOS) (Zhang et al., 2018b). The length of the growing season is defined as the number of days between greenup onset and dormancy onset.

The HPLM has various advantages over other algorithms, for example: (1) it offers a simple and continuous function for modeling the vegetation increase and decrease processes; (2) it identifies phenological transition dates without predefined thresholds (Zhang, 2018); (3) it fits remotely sensed phenological development better than both Fourier-based and asymmetric Gaussian functions (Beck et al., 2006), and produces more reliable phenological retrievals than the penalized cubic smoothing spline algorithm (Roman et al., 2024; Tian et al., 2021b) because the logistic function can remove noise effectively by relying on the temporal shape of vegetation growth; and (4) it provides global applications in operational VIIRS global phenology product generation (Zhang et al., 2024), as extensively validated using in situ observations from national phenology networks (Ye et al., 2022), near surface PhenoCam observations (Zhang et al., 2018a), 30 m phenometrics from dense time series of Landsat data (Moon et al., 2019; Zhang et al., 2017) and HLS-PhenoCam time series (Roman et al., 2024). However, the HPLM algorithm remains challenging when simulating irregular greenness trajectories in drylands.

3.1.2. Enhanced hybrid piecewise logistic model (E-HPLM)

Due to the irregular rainy and dry episodes and the heterogeneous plant growing cycles in drylands, vegetation greenness quantified by EVI2 often shows multiple plateau stages in a greenup or senescence phase and long linear tails before or after a growing season. Such a temporal EVI2 trajectory cannot be properly simulated using a single logistic model. Thus, in this study, we made two major changes to the HPLM algorithm to develop the enhanced HPLM (E-HPLM) algorithm after preprocessing the EVI2 time series. First, we designed an algorithm to assess whether plateau stages occurred in a phenological phase. The plateau stage was defined as a period with stable or slight changes in the vegetation greenness values. Specifically, a plateau stage should satisfy the three conditions in Eq. (2) (Fig. 2a–c), which can be described as follows. (1) The change in EVI2 in the full plateau stage should be smaller than 2 % of the seasonal magnitude, which is determined based on the uncertainty of the EVI2 values. It is widely accepted that the uncertainty in VIIRS (or MODIS) NDVI and EVI is 0.02 ± 0.02 (Fontana et al., 2009; Miura et al., 2000; Skakun et al., 2018). As a result, a variation of less than 2 % of the magnitude does not reflect an actual increase or decrease in photosynthetic activities within a satellite pixel. (2) The change in EVI2 between two neighboring points (3-day EVI2) should be continuously smaller than 0.5 % of the seasonal magnitude. Based on our sensitivity analysis, the EVI2 rate varies from 0.0004 to 0.012 EVI2/day if the seasonal EVI2 magnitude ranges from 0.05 to 0.7 and the phase duration from 60 to 120 days. However, the 0.5 % threshold leads to an EVI2 rate varying from 0.00001 to 0.0012 EVI2/day, which is also much smaller than the EVI2 uncertainty. This means that the 0.5 % threshold indicates a negligible increase or decrease pattern between two neighboring observations and is sufficient to determine the period without regular vegetation growth. (3) The plateau stage should be longer than two weeks since uncertainties associated with artifacts often occur in daily or 3-day satellite observations and regular vegetation growth stages are shorter than one week (Ammar and Davies, 2019; Reeves et al., 2001).

$$\left\{ \begin{array}{l} |y_n - y_{n-1}| < 0.005 \times H, n \in [0, m] \\ |y_m - y_0| < 0.02 \times H \\ |x_m - x_0| > 14 \text{ days} \end{array} \right. \quad (2)$$

where H is the magnitude of a growing cycle, m is the number of 3-day EVI2 points within a plateau stage, (x_0, y_0) is the starting point of a plateau stage, and (x_m, y_m) is the ending point of a plateau stage.

The sub-stages during a vegetation growing phase were bisected using the middle points of the determined plateau stages (Fig. 2). For a

greenup phase or senescence phase, two EVI2 segments were applied if one plateau was observed, while three segments were used for two plateaus. For each segment (or sub-stage), the logistic model (Eq. (1)) was applied to fit the EVI2 values. All of the fitted segments were used to generate a continuous EVI2 time series for a greenup (or senescence) phase, with an overall increasing (or decreasing) trajectory. In this case, there were more than three extreme points in the temporal curvature change rate for each growing phase, in which the dates corresponding to the earliest and latest extreme points were respectively defined as the greenup onset and maturity onset during the greenup phase, and the senescence onset and dormancy onset during the senescence phase.

Next, we designed an algorithm to determine the existence of a linear tail before and after a growing season. A linear tail was defined as the phenomenon of very slow change with a linear pattern in the period with smaller EVI2 (Fig. 2d). Although the biophysical impacts are not fully understood, this phenomenon occurs frequently in drylands (Liu et al., 2017c; Liu et al., 2024). To determine whether a potential linear tail existed, a threshold of 15 % seasonal EVI2 magnitude was used, since a magnitude of 15–20 % of EVI2 (or NDVI) is commonly applied to determine the date of greenup onset or dormancy onset (Gray et al., 2019; Hargrove et al., 2009; Xie et al., 2022). Thus, the occurrence of a linear tail should meet the conditions in Eq. (3), which state that the observations should (Fig. 2d): (1) be located within the 15 % of small observations in a growing cycle, (2) have a period longer than three weeks, and (3) change slowly with a significant linear pattern.

$$\left\{ \begin{array}{l} y_{min} < y_n \leq y_{min} + 0.15 \times H, n \in [0, m] \\ |x_m - x_0| > 21 \text{ days} \\ |k1| < 0.002 \\ R^2 > 0.95 \text{ and } RMSE/Mean < 0.1 \end{array} \right. \quad (3)$$

where H is the magnitude of a growing cycle, y_{min} is the minimum EVI2 in a phenological phase, m is the number of 3-day EVI2 points within a linear tail, (x_0, y_0) is the starting point of a linear tail, and (x_m, y_m) is the ending point of a linear tail, $k1$ is the slope of the linear model for the 15 % of small EVI2 observations, and R^2 , $RMSE$, and $Mean$ are the coefficient of determination, root-mean-square-error (RMSE) and mean of the linear model for the 15 % of small EVI2 observations, respectively.

For a growing phase with a linear tail, a linear parameter was added to the logistic function to tune the curve fitting. It was assumed that the linear parameter could model the slow change before and after the growing season. Thus, the logistic function was modified as follows:

$$EVI2(t) = \frac{EVI2_{amplitude} + d \times t}{1 + e^{a+b \times t}} + h \times t + EVI2_{background} \quad (4)$$

where h is related to the gradual and linear changes at the tail of a phase ($h = 0$ if no linear tail exists).

Theoretically, we could use Eq. (4) to fit all the time series without setting the conditions in Eq. (3). The specific process involves comparing the curve fitting with and without the linear term and then selecting the better fitting. However, to avoid any potential uncertainties and reduce the computation time, we only applied Eq. (4) to the pixels that showed a potential linear tail, and the linear term was not used otherwise.

As a result, in the implementation of regional or global LSP detections, the E-HPLM algorithm automatically checks if plateaus or linear tails exist in a pixel time series. If the existence occurs, E-HPLM is applied; otherwise, HPLM is automatically selected.

3.2. Retrievals of E-HPLM phenometrics

We examined the performance of E-HPLM at three spatial scales. At the PhenoCam site level, the E-HPLM algorithm was applied to the PhenoCam 3-day GCC time series (Section 2.5) to derive the PhenoCam phenometrics (hereafter termed PhenoCam E-HPLM). For comparison purposes, we also generated reference PhenoCam phenometrics using the HPLM algorithm (hereafter termed PhenoCam HPLM). At the

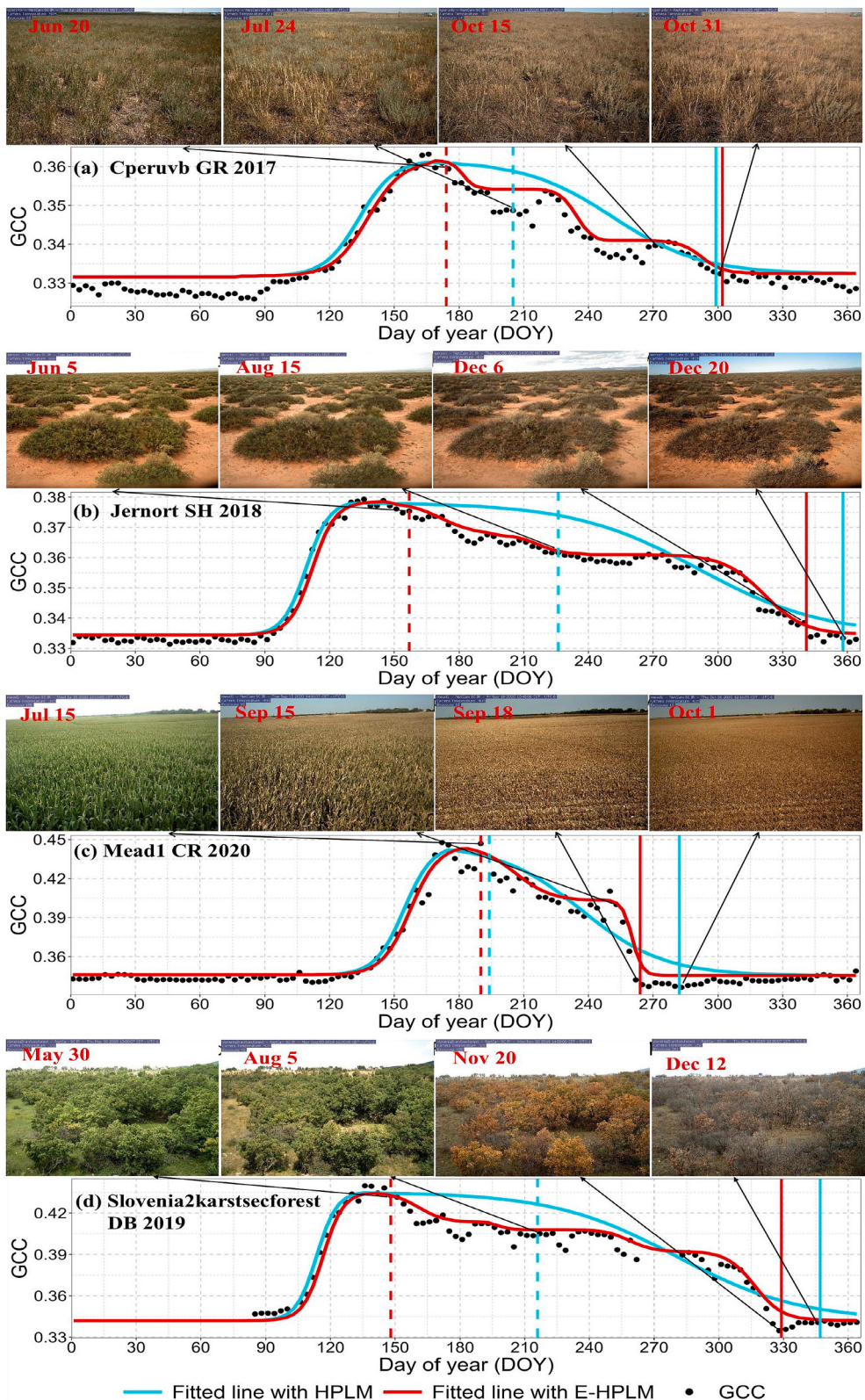


Fig. 3. Results for the E-HPLM and HPLM retrievals of phenology at four selected PhenoCam sites. Vertical lines indicate senescence onset (dashed) and dormancy onset (solid) obtained from E-HPLM (red) and HPLM (cyan). GCC: green chromatic coordinate, GR: grasslands, SH: shrublands, CR: croplands, DB: deciduous broadleaf. (For interpretation of the references to colour in this figure legend, the reader is referred to the web version of this article.)

regional level (30 m pixels around PhenoCam sites), the E-HPLM algorithm was applied to the 3-day EVI2 time series from HLS-PhenoCam fusion data (Section 2.6) to derive the HLS-PhenoCam phenometrics (hereafter termed HLS-PhenoCam E-HPLM). We note that the HLS-PhenoCam HPLM dataset at 30 m pixels was generated previously, and was available from the ORNL DAAC (Section 2.6).

The VIIRS 3-day EVI2 time series was also preprocessed at the global scale following the HPLM algorithm described in Section 3.1. The E-HPLM algorithm was then applied to derive the VIIRS global phenometrics from 2013 to 2022 (hereafter termed VIIRS E-HPLM).

3.3. Evaluation of phenometrics retrieved from E-HPLM

The E-HPLM phenometrics were evaluated using five different datasets. First, the E-HPLM was examined to fit the GCC time series at PhenoCam sites since the PhenoCam imagery allowed us to visualize the stages of vegetation growth. Specifically, we selected four sites showing irregular temporal trajectories of vegetation growth, including at least one plateau stage in the time series. The four sites were dominated by different types of vegetation, and consisted of three sites in the western CONUS (cperuvb site: grasslands in 2017, jernort site: shrublands in 2018, and mead1site: croplands in 2020), and one site from Europe (slovenia2karstsecforest site: deciduous broadleaf forests mixed with grasses in 2019). Both HPLM and E-HPLM were applied to fit the GCC time series and derive the phenometrics separately. The agreement between the raw observations and the fitted values was assessed based on the RMSE. The derived phenological dates were examined by visualizing PhenoCam imagery, which allowed us to identify the most likely dates of phenological events (leaf emergence, maximum, senescence, and drop) and then compare them with the modeled phenological dates.

Next, we examined the E-HPLM in regard to fitting the VIIRS EVI2 time series. Specifically, we randomly selected four VIIRS pixels from tile h08v05 located in the western CONUS in 2019, and fitted the EVI2 time series using HPLM and E-HPLM separately. The RMSE was calculated to measure the difference between the raw EVI2 and the fitted EVI2

values.

In the third step, we identified pixels where LSP retrievals could be potentially improved by using E-HPLM across global drylands. This was performed by counting the number of years for which plateau stages and linear tails existed in the EVI2 time series during 2013–2022. The calculations were separated for the greenup and senescence phases. We also calculated the average number of years with plateau stages for four major types of land cover (grasslands, savannas, shrublands, and croplands). We then conducted a comparison between E-HPLM and HPLM retrievals at the global scale for five phenometrics. Each of the phenometrics from 2003 to 2022 was averaged, and the difference between E-HPLM and HPLM retrievals was calculated for individual pixels. Note that a phenological event retrieved from E-HPLM and HPLM could be in two calendar years, due to uncertainties in the algorithms (for example DOY 360 in the preceding year from one algorithm and DOY 5 in the current year from another algorithm, leading to a difference of 10 days). To calculate the differences in a phenological event in the current year retrieved from these two algorithms, we calculated the differences among all the paired events within three years and then used the smallest values to identify the actual pairs of phenological events. We also compared the linear trends for VIIRS phenometrics between E-HPLM and HPLM retrievals. This comparison was performed for pixels that met the following criteria: (1) having plateau stages or linear tails for at least one year during 2013–2022, and (2) showing significant linear trends (p -value <0.01 in the t -test) during 2013–2022.

Furthermore, we evaluated the performance of E-HPLM in terms of fitting the VIIRS EVI2 time series using the agreement index (Zhang, 2015):

$$\text{Agreement index} = 100 - \frac{\sum_{i=1}^n (y_i - o_i)^2}{\sum_{i=1}^n (|y_i - \bar{o}| + |y_i - \bar{o}|)^2} \times 100\% \quad (5)$$

where n is the number of 3-day VIIRS EVI2 observations with high quality, y_i is the modeled EVI2 value, o_i is the observed high-quality

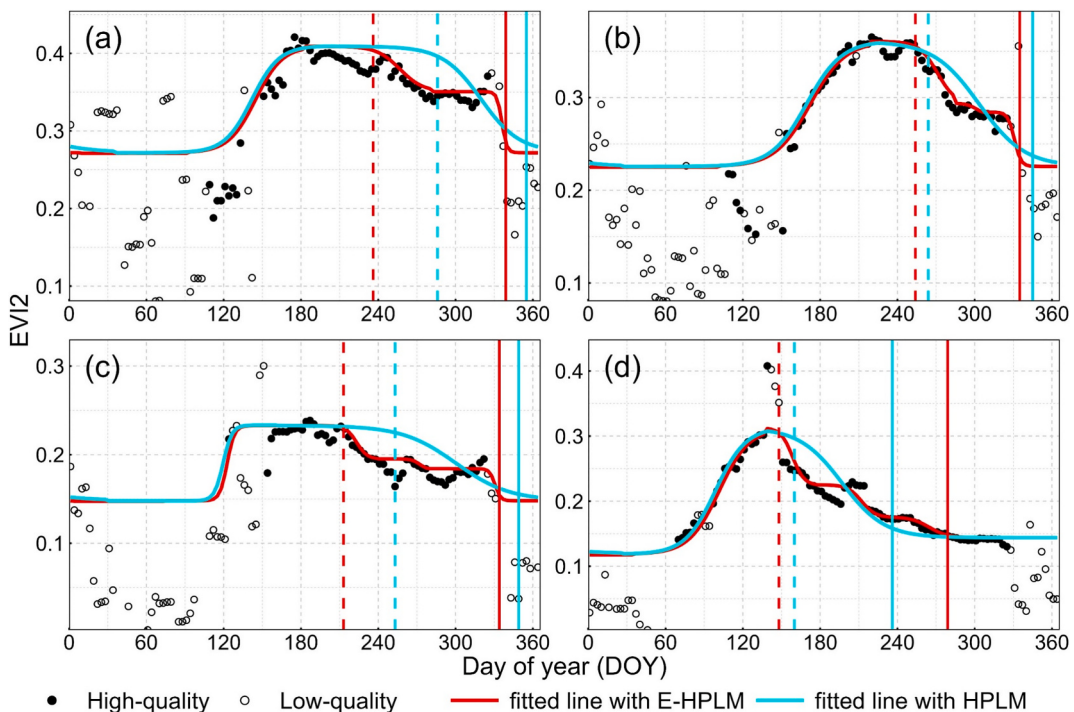


Fig. 4. Examples of VIIRS pixels randomly selected from the State of Nevada in the United States (tile h08v05, 2019), showing large differences in dormancy onset between the E-HPLM and HPLM retrievals. Vertical lines indicate senescence (dashed) and dormancy (solid) onset dates obtained from E-HPLM (red) and HPLM (cyan). (For interpretation of the references to colour in this figure legend, the reader is referred to the web version of this article.)

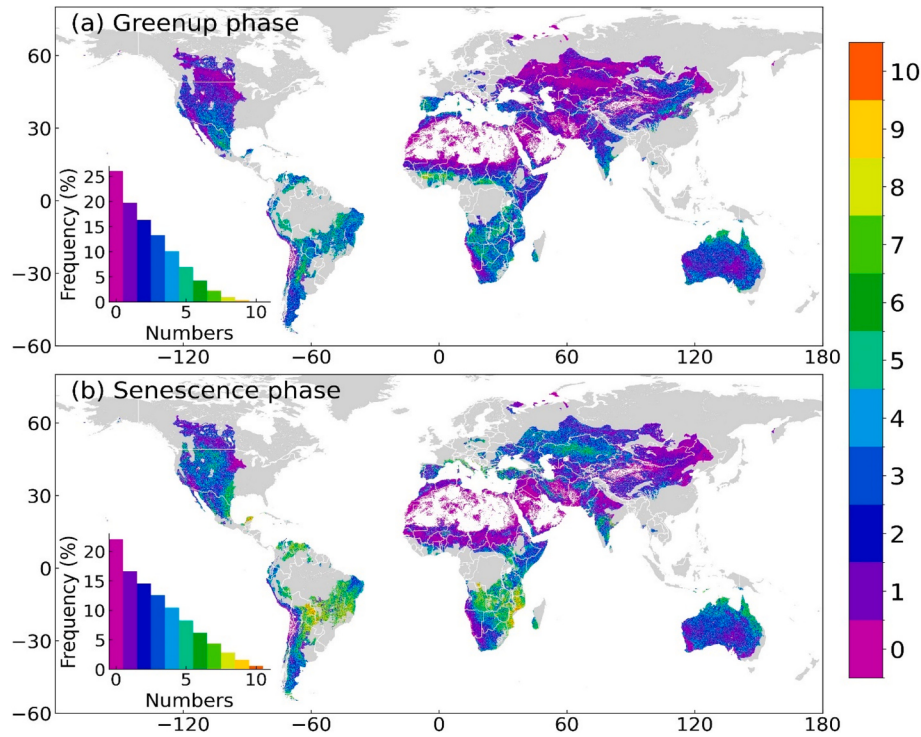


Fig. 5. Number of years with plateau stages in the (a) greenup phase and (b) senescence phase in VIIRS EVI2 time series across drylands during 2013–2022. Non-dryland pixels are represented in gray. The numbers on the X- and Y-axes indicate degrees of longitude and latitude, respectively.

EVI2 value, and \bar{o} is the mean value of o_i .

The agreement index has a range of 0–100%, where 0% indicates complete disagreement between modeled and observed values and 100% indicates equality between the modeled and observed values (Zhang, 2015). The agreement from 2003 to 2022 was averaged in four different ways, using: (1) all valid pixels, (2) pixels with plateau stages but no linear tails during a growing season, (3) pixels with linear tails but no plateau stages during a growing season, and (4) pixels with both plateau stages and linear tails during a growing season.

In the fourth step, we evaluated the E-HPLM derived VIIRS phenometrics using the E-HPLM derived PhenoCam phenometrics for 132 PhenoCam sites (294 site-years). For all of these site-years, the corresponding VIIRS EVI2 time series showed irregular variations, which contained either plateau stages or linear tails. As a reference, the HPLM-derived VIIRS phenometrics were also compared with HPLM-derived PhenoCam data. Since different algorithms could produce different results, it would be more reasonable to compare the results retrieved from VIIRS and PhenoCam observations using the same algorithm. Their differences were measured using the mean absolute difference (MAD), bias, and correlation coefficient (R).

Finally, we evaluated the E-HPLM derived VIIRS phenometrics using the 36 samples of $10 \times 10 \text{ km}^2$ HLS-PhenoCam data that were retrieved from the HLS-PhenoCam EVI2 time series using the E-HPLM algorithm. As a reference, the HPLM-derived VIIRS phenometrics were also compared with HPLM-derived HLS-PhenoCam data. To do this, the 30 m HLS-PhenoCam phenometrics were first aggregated to 500 m using the average method, and then compared with VIIRS phenometrics using the MAD, bias, R , and linear regression. Only VIIRS pixels with irregular EVI2 trajectories that contained either plateau stages or linear tails were considered for analysis. To explore the impacts of spatial heterogeneity on phenological retrieval, we also calculated the standard deviation (SD) of HLS-PhenoCam phenometrics in a VIIRS pixel. The SD in VIIRS pixels was averaged with two scenarios: (1) no plateau stages or linear tails, and (2) observed plateau stages or linear tails. The MAD between VIIRS E-HPLM and HPLM retrievals against SD was determined.

4. Results

4.1. Fitted temporal trajectory of vegetation growth

The E-HPLM and HPLM algorithms performed differently when fitting irregular PhenoCam GCC trajectories during the vegetation growth (Fig. 3). E-HPLM was able to track multiple growth stages during a growing phase, whereas HPLM showed one single sigmoidal shape, although both models gave a similar end to the growing cycle in some cases (such as dormancy onset in Fig. 3a). The RMSE values for the raw and fitted GCC time series were 0.003 and 0.005 for E-HPLM and HPLM, respectively, at site cperuvb, 0.002 and 0.006 at site jernort, 0.007 and 0.009 at site mead1, and 0.007 and 0.015 at site slovenia2karstseforest. Some of the retrieved phenological dates had a difference larger than two months at senescence onset (Fig. 3b, d) and half a month at dormancy onset (Fig. 3b–d). However, E-HPLM and HPLM produced similar results when fitting the GCC time series and retrieving the greenup onset and maturity onset, since no plateau stages existed during the spring phase (Fig. 3).

The difference between E-HPLM and HPLM was further explored by fitting four VIIRS EVI2 time series that were randomly selected from tile h08v05 (in the western CONUS) in 2019 (Fig. 4). This clearly showed that phenometrics were strongly impacted by fitting behaviors. Due to the existence of plateau stages, the dormancy onset from E-HPLM was retrieved as 10–16 days earlier than the same onset from HPLM at three sites (Fig. 4a–c), while it was delayed by 43 days at another site (Fig. 4d). The senescence onset date also showed a large difference, being 50 and 40 days earlier in the E-HPLM than HPLM retrievals at two sites (Fig. 4a, c), respectively. E-HPLM showed an obvious advantage over HPLM in reducing the bias in fitting the time series. The RMSE between raw (high-quality) and fitted EVI2 values was 0.005–0.01 smaller for E-HPLM than for HPLM for these four examples.

Table 3

Proportion (%) of pixels and number of years with plateau stages in VIIRS EVI2 time series during 2013–2022 for different dryland categories and land cover types (land cover types obtained from the MCD12Q1 product).

Drylands	Land cover types	Greenup phase		Senescence phase	
		Proportion of pixels (%)	Number of years	Proportion of pixels (%)	Number of years
Hyper-arid areas	Grasslands	0.10	2.7	0.11	3.2
	Savannas	0.01	2.8	0.01	4.2
	Shrublands	0.11	2.4	0.12	3.0
	Croplands	0.05	3.2	0.04	3.1
Arid areas	Grasslands	3.31	2.2	4.15	3.0
	Savannas	0.10	3.4	0.14	4.1
	Shrublands	6.10	2.4	6.24	2.5
	Croplands	0.34	2.5	0.29	2.6
Semi-arid areas	Grasslands	14.92	2.2	16.03	2.4
	Savannas	2.57	3.5	2.90	4.5
	Shrublands	6.04	3.5	5.92	3.5
	Croplands	3.39	2.3	3.14	2.6
Dry sub-humid areas	Grasslands	4.75	3.5	4.77	3.9
	Savannas	4.31	3.2	5.04	4.0
	Shrublands	0.53	4.1	0.55	4.2
	Croplands	3.79	2.7	4.00	2.7
Additional areas	Grasslands	5.60	3.7	5.41	4.0
	Savannas	4.75	4.1	4.88	6.0
	Shrublands	0.26	3.9	0.24	4.0
	Croplands	1.13	3.2	0.94	3.2

4.2. Spatial distribution of pixels with irregular EVI2 time series in global drylands

The occurrence of irregular EVI2 time series with plateau stages varied in the greenup and senescence phases during 2013–2022 (Fig. 5). Plateau stages occurred at least once in 74 % of the greenup phase and 78 % of the senescence phase across the dryland areas over the 10-year period, with a yearly range of 27–29 % in the greenup phase and 33–35 % in the senescence phase. In contrast, the linear tail in the EVI2 time series only occurred in a very small number of pixels, with 0.7 % in the greenup phase and 0.8 % in the senescence phase, meaning that the distribution of pixels was too sparse to be shown here.

The frequency of the plateau stages varied with the dryland category and land cover type (Table 3). Plateau stages appeared more frequently with an increase in humidity, as defined by the aridity index. The mean number of years for a pixel with plateau stages was 2.3, 2.6, 3.2, and 3.8 in arid areas, semi-arid areas, dry sub-humid areas, and additional areas, respectively, in the greenup phase, with values of 2.7, 2.9, 3.6, and 4.8, respectively, in the senescence phase. Of the different land cover types, plateau stages appeared most frequently in savannas, followed by shrublands, grasslands, and croplands. The mean number of years with plateau stages for these four land cover types (grasslands, savannas, shrublands, and croplands) was 3.6, 3.0, 2.7, and 2.6, respectively, in the greenup phase, while the values were 4.9, 3.1, 3.0, and 2.7, respectively, in the senescence phase. Based on a combination of the land cover types and dryland categories, it was determined that

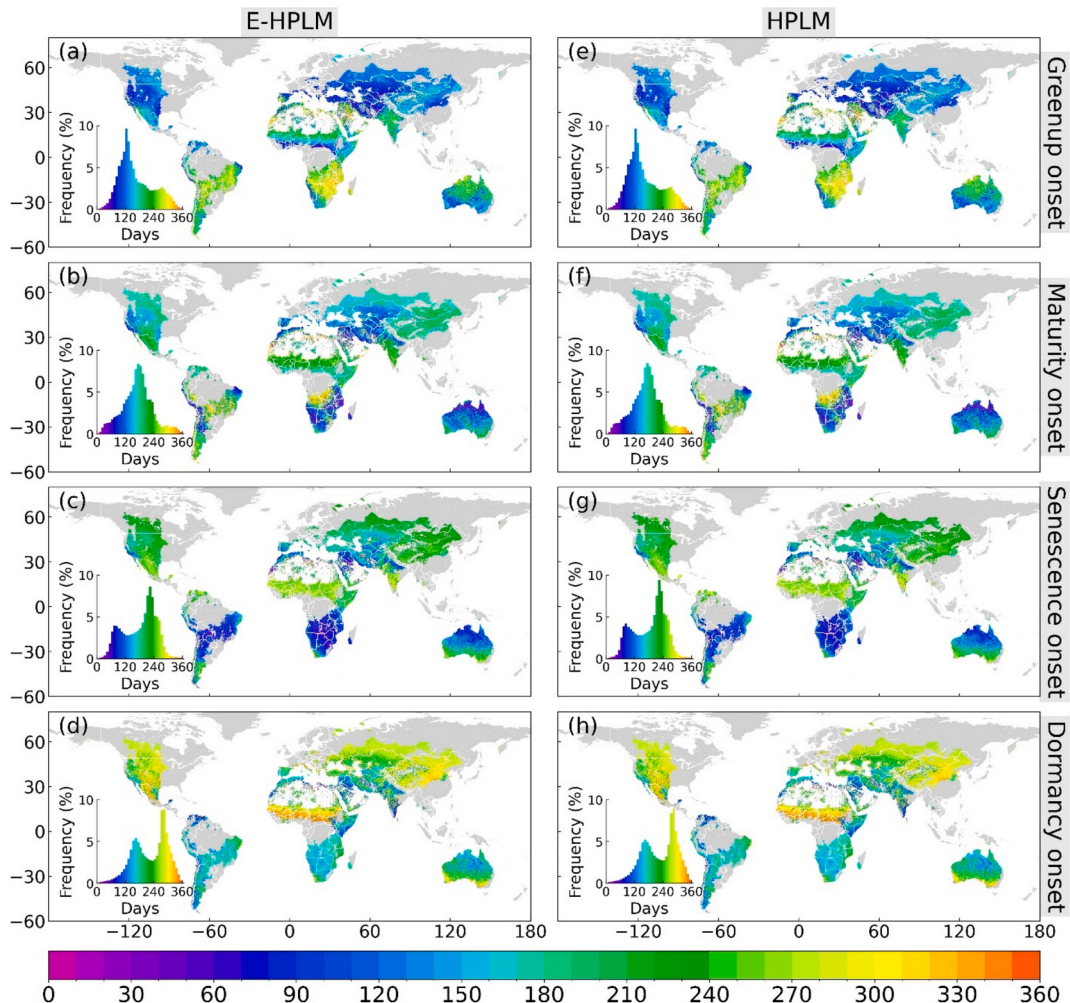


Fig. 6. VIIRS key phenometrics (day of year, DOY) retrieved from (a–d) E-HPLM and (e–h) HPLM. Values were averaged over 2013–2022. Non-dryland pixels are represented in gray. The numbers on the X- and Y-axes indicate degrees of longitude and latitude, respectively.

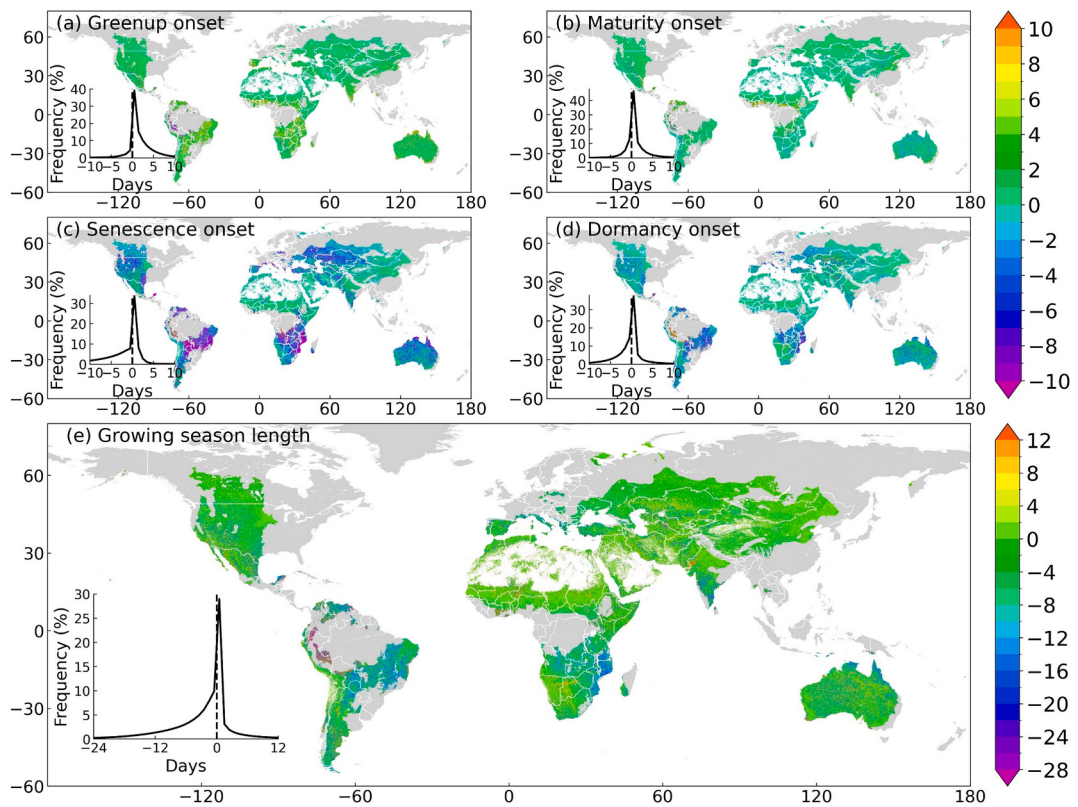


Fig. 7. Differences (days) in VIIRS key phenometrics between E-HPLM and HPLM retrievals. The differences were calculated by subtracting HPLM from E-HPLM after phenometrics were averaged over 2013–2022. Non-dryland pixels are represented in gray. The numbers on the X- and Y-axes indicate degrees of longitude and latitude, respectively.

savannas in the drylands of additional areas experienced the highest frequency of plateau stages, with values of 4.1 years in the spring phase and 6.0 years in the senescence phase. In contrast, grasslands in semi-arid areas showed the lowest frequency, with 2.2 and 2.4 years in the spring and senescence phases, respectively. However, grasslands in semi-arid areas accounted for the largest proportion (15.5 %) of global dryland pixels.

4.3. Comparison of E-HPLM phenometrics with the HPLM-retrieved VIIRS GLSP product

Phenometrics retrieved from E-HPLM showed some differences from the HPLM-retrieved VIIRS GLSP product for global drylands from 2013 to 2022. Overall, their spatial patterns were similar, without distinctive discrepancies (Fig. 6). The values of MAD between the two model retrievals were 2.3, 1.9, 4.4, and 2.9 days for greenup onset, maturity onset, senescence onset, and dormancy onset, respectively (Fig. 7a–d). These small differences were as expected, since both models produced the same values for pixels without plateau stages and linear tails during a given phenological phase. For pixels with irregular EVI2 time series that contained either plateau stages or linear tails, however, the MAD values for the four phenometrics were 9.1, 8.5, 13.7, and 9.8 days, respectively. Compared with HPLM, E-HPLM gave a later greenup onset (81.4 % of pixels) and an earlier dormancy onset (75.0 % of pixels), resulting in a shorter growing season (81.5 % of pixels) (Fig. 7e). Globally, the MAD for the growing season length was 5.1 days for all pixels, whereas it was 14.8 days for pixels with irregular EVI2 time series.

A trend analysis indicated that the linear slopes in the VIIRS phenometrics showed no obvious difference between E-HPLM and HPLM retrievals from 2013 to 2022 (Fig. 8). In drylands, only ~0.3 % of pixels showed a significant linear trend (p -value <0.01 in the T-test). Of these

pixels, over 99 % showed the same direction for the E-HPLM and HPLM retrievals, although large deviations were found for a small number of pixels.

The agreement index revealed that E-HPLM fitted the EVI2 time series better than HPLM (Fig. 9). The global agreement index increased from 83 % (HPLM) to 85 % (E-HPLM) for all the pixels during 2013–2022, and the proportion of pixels with a high agreement index (> 90 %) increased by 10 %. Moreover, the improvement was different for pixels with plateaus and linear tails (Fig. 10). The agreement index for EVI2 fitted with E-HPLM increased by ~4 % for pixels with plateaus and ~ 3 % for pixels with linear tails. However, the increase in the agreement index for pixels with plateaus only was close to those with either plateaus or linear tails, indicating that pixels with plateau stages were predominant.

4.4. Evaluation of E-HPLM using PhenoCam data

E-HPLM produced a higher agreement between VIIRS and PhenoCam LSP retrievals than HPLM. Overall, the E-HPLM retrievals yielded a correlation (R^2) of 0.63–0.69 and a MAD of 20–26 days for different phenological events, while the HPLM retrievals had an R^2 of 0.54–0.65 and an MAD of 22–28 days. This indicated that E-HPLM had a higher R^2 (0.02–0.1 increase) and smaller MAD (reduction of one to three days) than HPLM for the four phenometrics (Fig. 11). E-HPLM produced a similar MAD (< 0.5 days) to HPLM for greenup onset in grasslands, maturity onset in croplands, and senescence onset in evergreen needleleaf forests (Table 4). However, large differences in MAD were observed for greenup onset in evergreen needleleaf forests (five days) and dormancy onset in deciduous broadleaf forests (six days). Across different types of drylands, E-HPLM gave reduced values of MAD in comparison with HPLM, especially for semi-arid areas. The MAD was reduced by about three days on average in semi-arid areas and six days

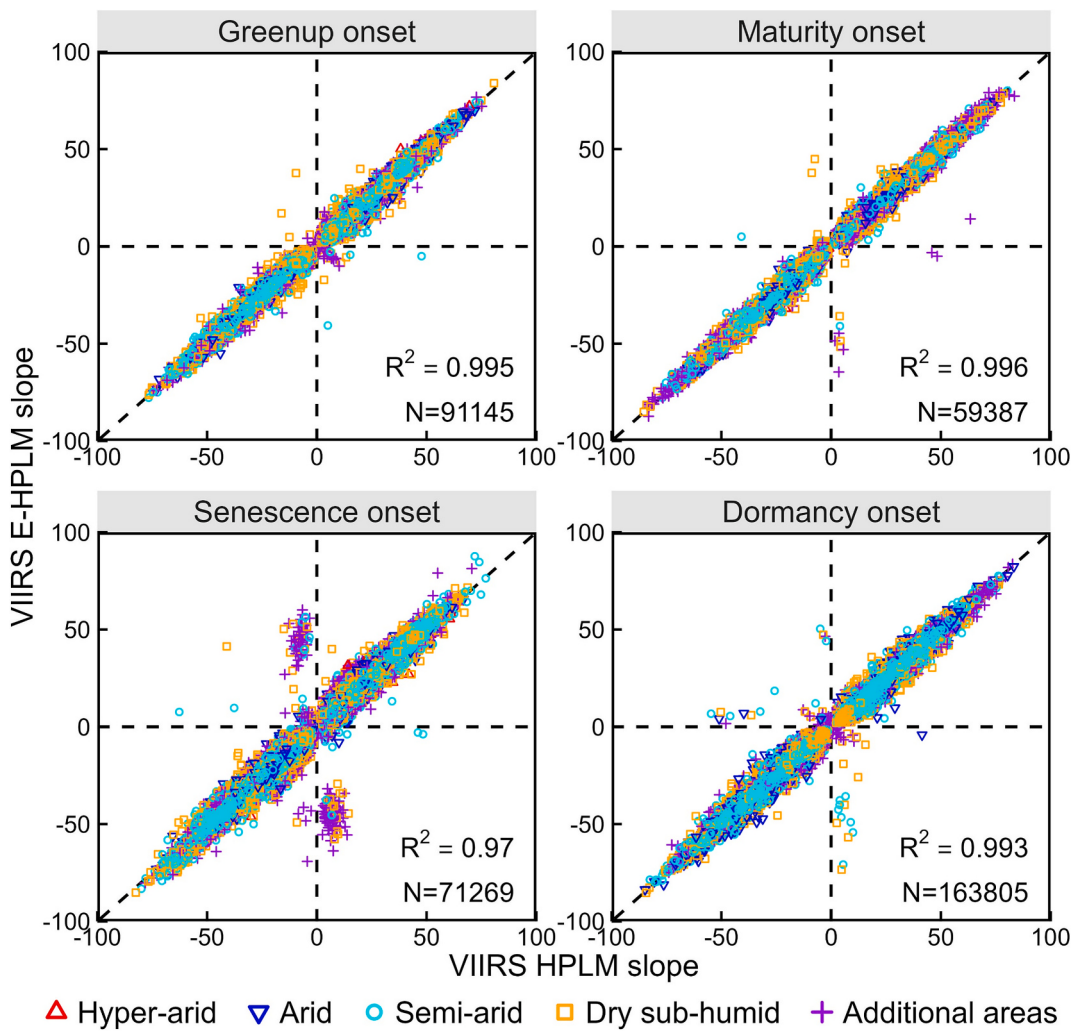


Fig. 8. Comparison of linear slopes (day/year) for VIIRS phenometrics obtained from E-HPLM and HPLM retrievals for 2013–2022 in drylands. Only pixels with significant trends (p -value <0.01 in the t -test) are shown.

for senescence onset in additional areas (Table 5). The reduction in MAD obtained with E-HPLM was less than three days for the other phenometrics and aridity types.

4.5. Evaluating E-HPLM using HLS-PhenoCam data

Fig. 12 shows a comparison between the VIIRS and HLS-PhenoCam LSPs retrieved using E-HPLM and HPLM. The MAD for the E-HPLM retrievals ranged from 18 to 21 days for the four phenological dates, while the MAD for the HPLM retrievals ranged from 19 to 24 days. These results demonstrated that E-HPLM had a smaller MAD (one to two days less) than HPLM for all four phenometrics. The difference in MAD was generally largest for the shrublands, with values of two days for greenup onset, six days for maturity onset, and three days for dormancy onset (Table 6). It was followed by grasslands and croplands, which showed the largest differences of three days and two days, respectively, in senescence onset. E-HPLM also gave a smaller MAD between the VIIRS LSP and HLS-PhenoCam retrievals than HPLM across different types of aridity (Table 7). The difference in MAD between the E-HPLM and HPLM retrievals was largest for the dryland type of additional areas, with values of two days for greenup onset, and five days for both maturity onset and senescence onset. The largest difference in MAD was seen for maturity onset for all aridity types.

Fig. 13 reveals that the phenological heterogeneity within the VIIRS pixels impacted the MAD between the E-HPLM and HPLM retrievals. The

standard deviation (SD) in the HLS-PhenoCam phenometrics, representing spatial heterogeneity, was three to six days larger for the VIIRS pixels with plateau stages or linear tails in the EVI2 trajectories than for those with regular EVI2 time series (Fig. 13a). With an increase in heterogeneity, the MAD for the VIIRS phenometrics between E-HPLM and HPLM retrievals increased linearly with $SD < 25$, and showed relatively stable behavior for $SD > 25$; the exception was for senescence onset, where the MAD still showed linear patterns of increase but with reduced slopes (Fig. 13b).

5. Discussion

In this study, a method of enhancing HPLM was developed to trace the irregular seasonal trajectories of vegetation growth. Unlike vegetation in humid ecosystems, where the greenness of the vegetation increases or decreases gradually and continuously during a growing season, vegetation in drylands commonly experiences irregular variations, since precipitation is the major driver of plant phenology (Currier and Sala, 2022; Ma et al., 2013; Zhang et al., 2005). Vegetation greenness in drylands increases gradually after a rainfall event, but may remain either unchanged or decrease slightly in a dry episode, and may increase again if another rainfall event occurs. This phenomenon results in unique characteristics of the VI time series, with plateau stages and linear tails. Moreover, the species and abundances of vegetation may be spatially very heterogeneous in drylands. As a result, the temporal

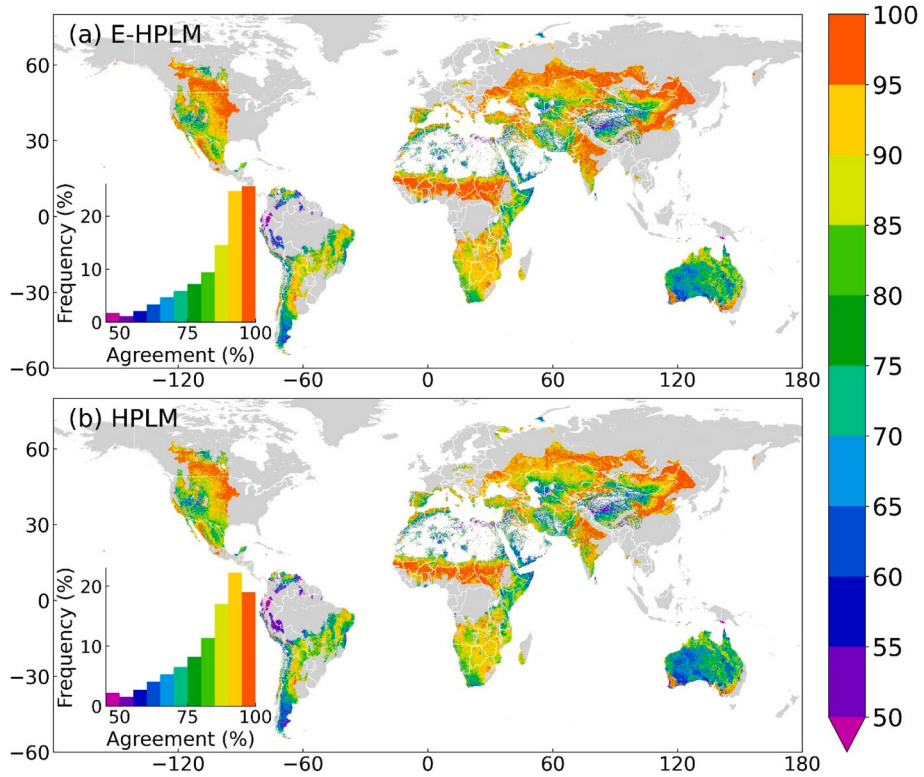


Fig. 9. Agreement index (%) for fitting of EVI2 time series using (a) E-HPLM and (b) HPLM. Values were averaged over 2013–2022. Non-dryland pixels are represented in gray. The numbers on the X- and Y-axes indicate degrees of longitude and latitude, respectively.

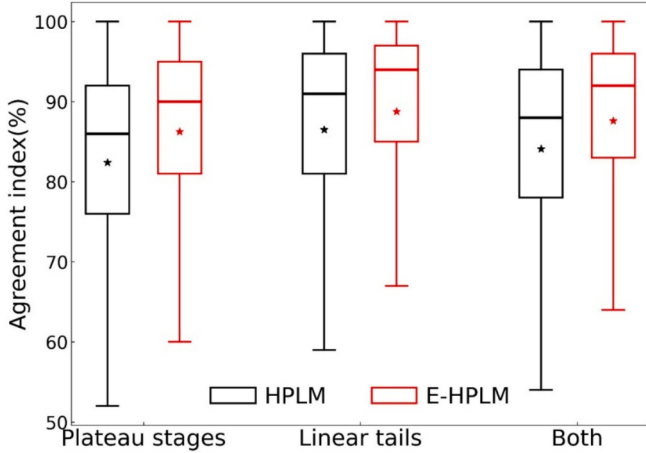


Fig. 10. Statistical results for the agreement index (%) for fitting of EVI2 time series using E-HPLM and HPLM during 2013–2022. Stars represent mean values. Plateau stages: pixels have plateau stages in a growing season but no linear tails. Linear tails: pixels have linear tails in a growing season but no plateau stages. Both: pixels have both plateau stages and linear tails in a growing season.

trajectories of vegetation greenness within a satellite pixel with heterogeneous vegetation species may be complex. The proposed E-HPLM algorithm, with biophysically meaningful models to describe temporal greenness patterns, has a demonstrated capability to describe the complexity of temporal vegetation greenness development. This is significantly distinguished from a recently proposed dryland phenology retrieval method that simply uses thresholds from spline-interpolated and Savitzky-Golay-filtered EVI2 time series (Dong et al., 2025), which is hard to capture well the irregular vegetation growth cycles.

E-HPLM showed better performance than HPLM in terms of fitting the PhenoCam GCC and VIIRS EVI2 time series with plateau stages. A normal logistic growth curve in HPLM changes fastest in a monotonic way during the middle greenup and senescence phases, but cannot appropriately model phases with plateau stages (Figs. 3 and 4). HPLM frequently overestimated the length of a growing season by advancing the date of greenup onset and delaying the date of dormancy onset (Fig. 7). This result is partly supported by previous findings from the validation of LSPs using in situ observations, which showed that HPLM derived an earlier spring phenology (Tian et al., 2021a; Wu et al., 2016; Ye et al., 2022) and a later autumn phenology (Ganguly et al., 2010; Verma et al., 2016; Xie and Wilson, 2020). In contrast, E-HPLM offered flexibility in fitting the sub-phases separated by plateaus, and provided more accurate retrievals of phenological dates and estimates of greenness magnitudes, with a relatively high agreement index between the fitted and raw EVI2 (high-quality) values. The raw EVI2 reflects the vegetation productivity well.

The plateau stages appeared more frequently during the senescence phase than the greenup phase (Fig. 5 and Table 3). This phenomenon is likely associated with the fact that plant greenup was much faster, with a shorter duration than senescence. For example, the duration between greenup onset to peak greenness in California oak trees was about 20–40 days, while there was a period of around 4–5 months from senescence onset to dormancy onset (Liu et al., 2017c). Multiple rainy and dry episodes are likely to occur during a long period, and this could cause irregular trajectories with plateaus. As a result, HPLM was able to fit greenness variations better and to retrieve more accurate phenological dates in the greenup phases than in the senescence phases (Liu et al., 2023).

The plateau stages varied with land cover types and were most frequent in savannas and least frequent in croplands. Because savannas consisted of a mixture of grass and scattered woody plants (or trees), the high frequency of plateau stages in savannas may be explained by the asymmetric responses of grass and trees to water availability (rainfall).

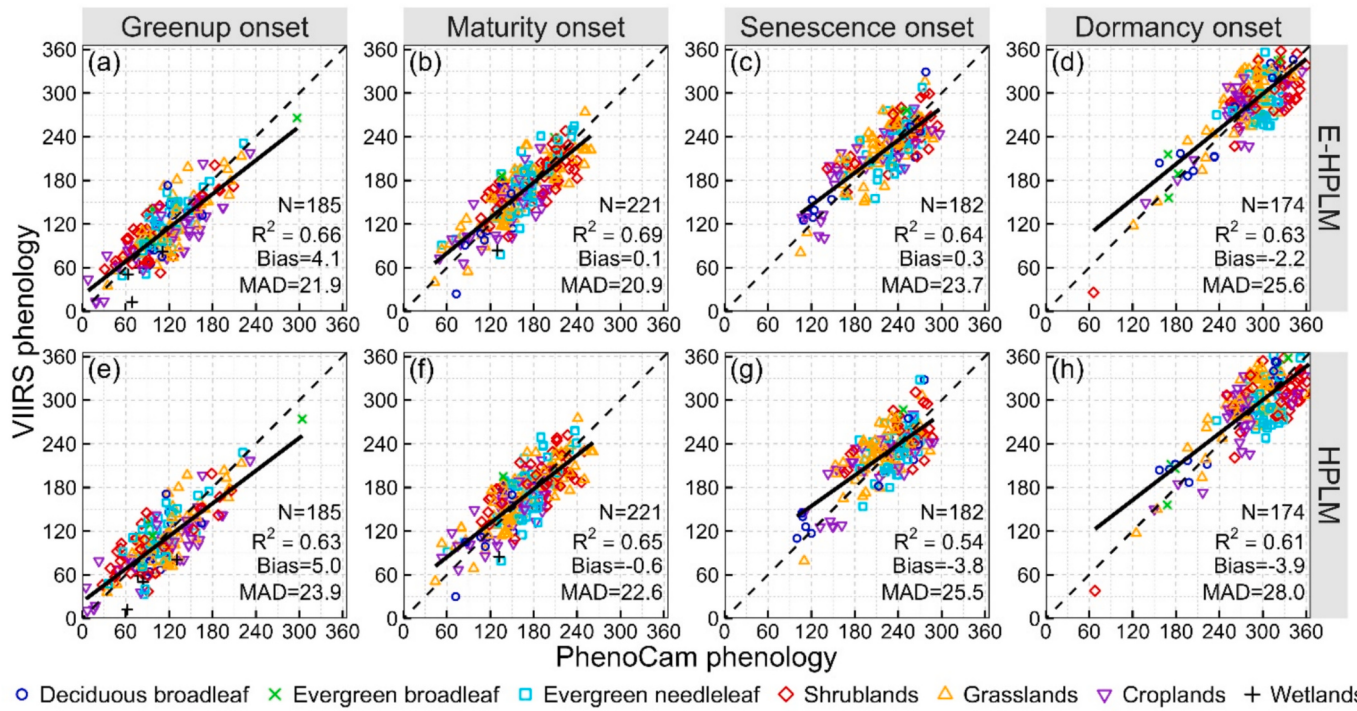


Fig. 11. Comparison between VIIRS phenology and PhenoCam phenology. (a-d) VIIRS and PhenoCam phenometrics retrieved from E-HPLM; and (e-h) VIIRS and PhenoCam phenometrics retrieved from HPLM. Only VIIRS pixels with either plateau stages or linear tails in the EVI2 time series were used. The X- and Y-axes show the phenological dates in the day of year.

Table 4

Mean absolute difference (MAD) between VIIRS and PhenoCam phenology retrieved from E-HPLM and HPLM for major vegetation types (Number > 10). Negative values indicate that E-HPLM produces lower MAD than HPLM. Vegetation types at PhenoCam sites: DB – deciduous broadleaf, EN – evergreen needleleaf, SH – shrublands, GR – grasslands, CR – croplands.

Phenometrics	Vegetation types	Number	MAD		
			E-HPLM	HPLM	Difference
Greenup onset	DB	11	24.8	26.5	-1.7
	EN	36	15.7	20.8	-5.1
	SH	35	24.7	27.5	-2.8
	GR	55	19.5	19.7	-0.2
	CR	41	26.5	27.0	-0.5
Maturity onset	DB	11	19.0	20.5	-1.5
	EN	44	19.7	23.1	-3.4
	SH	41	21.7	25.2	-3.5
	GR	84	19.5	20.4	-0.9
	CR	38	23.5	23.3	0.2
Senescence onset	DB	12	22.0	25.1	-3.1
	EN	38	23.1	23.1	0
	SH	38	24.1	24.1	0
	GR	64	22.4	25.3	-2.9
	CR	28	27.0	30.2	-3.2
Dormancy onset	DB	13	17.8	23.3	-5.5
	EN	31	26.4	29.2	-2.8
	SH	37	29.0	31.2	-2.2
	GR	57	24.9	26.1	-1.2
	AG	30	26.2	29.1	-2.9

Due to their deeper roots, the stronger water storage capacity in their stems, and their more diverse water conservation strategies (Walther et al., 2019), woody plants have stronger resistance and resilience than herbaceous plants to variations in precipitation (Currier and Sala, 2022) and soil water content (Zhang et al., 2016). Thus, the phenometrics for a single tree usually differ dramatically from those of its surroundings

Table 5

Mean absolute difference (MAD) between VIIRS and PhenoCam phenology retrieved from E-HPLM and HPLM for different drylands. Negative values indicate that E-HPLM produces lower MAD than HPLM.

Phenometrics	Drylands	Number	MAD		
			E-HPLM	HPLM	Difference
Greenup onset	Arid areas	13	24.8	27.2	-2.4
	Semi-arid areas	113	19.1	21.2	-2.1
	Dry sub-humid areas	34	22.2	22.7	-0.5
	Additional areas	25	33.0	36.1	-3.1
	Arid areas	19	23.4	25.5	-2.1
Maturity onset	Semi-arid areas	129	19.2	22.1	-2.9
	Dry sub-humid areas	43	22.3	21.6	0.7
	Additional areas	30	24.3	24.3	0
	Arid areas	16	22.8	22.0	0.8
	Semi-arid areas	104	23.7	25.8	-2.1
Senescence onset	Dry sub-humid areas	42	25.8	25.7	0.1
	Additional areas	20	19.6	26.0	-6.4
	Arid areas	18	30.2	31.4	-1.2
	Semi-arid areas	91	24.7	28.7	-4.0
	Dormancy onset	35	23.6	22.5	1.1
	Dry sub-humid areas	30	28.1	30.1	-2.0

(Cheng et al., 2020), as has been well-documented (Liu et al., 2017c). In addition, grazing by livestock and wildlife in the mid-season could also potentially drive the herbivory growth into plateau stages (Muthoka et al., 2022). The lower number of occurrences of plateau stages in croplands was most likely due to irrigation, as a sufficient water supply during the growing season leads to crops having a normal growth trajectory.

Across the different categories of dryland, pixels in which plateau stages occurred at least once during 2013–2022 were more widely

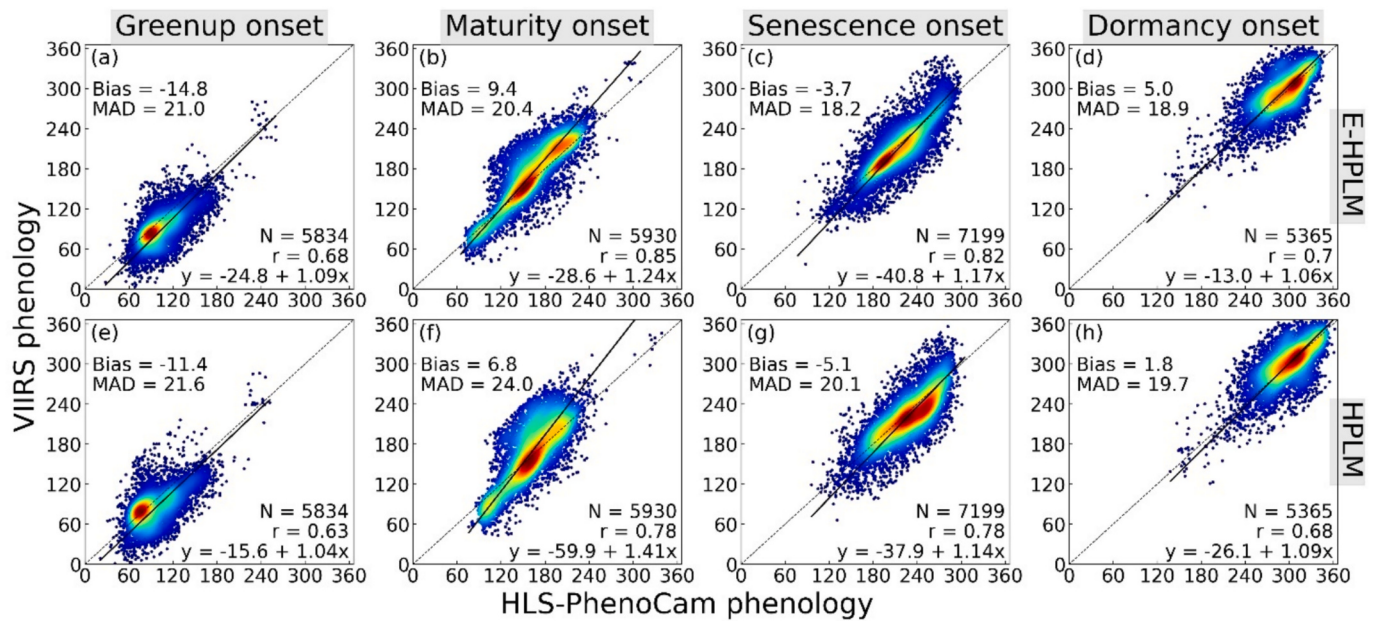


Fig. 12. Comparison between VIIRS and HLS-PhenoCam phenology. (a–d) VIIRS and HLS-PhenoCam phenometrics retrieved from E-HPLM; and (e–h) VIIRS and HLS-PhenoCam phenometrics retrieved from HPLM. Only pixels with either plateau stages or linear tails in EVI2 time series were used. Colors from blue to dark red indicate the density of pixels from low to high. (For interpretation of the references to colour in this figure legend, the reader is referred to the web version of this article.)

Table 6

Mean absolute difference (MAD) between VIIRS and HLS-PhenoCam phenology retrieved from E-HPLM and HPLM for the first three major land cover types. Land cover types obtained from the MCD12Q1 product. Negative values indicate that E-HPLM produces lower MAD than HPLM.

Phenometrics	Land cover types	Percentage (%)	MAD		
			E-HPLM	HPLM	Difference
Greenup onset	Grasslands	50.4	21.7	21.9	-0.2
	Shrublands	25.6	24.8	27.1	-2.3
	Croplands	15.1	16.8	16.9	-0.1
Maturity onset	Grasslands	56.7	18.5	22.7	-4.2
	Shrublands	19.9	31.4	37.0	-5.6
	Croplands	12.7	15.2	13.7	1.5
Senescence onset	Grasslands	63.6	17.3	19.9	-2.6
	Shrublands	16.9	23.8	23.9	-0.1
	Croplands	10.3	14.4	16.2	-1.8
Dormancy onset	Grasslands	64.7	20.0	20.5	-0.5
	Shrublands	15.2	16.0	18.9	-2.9
	Croplands	12.1	15.5	15.5	0

distributed in semi-arid areas than in other areas. However, for those pixels, the frequency (number of years) of plateau stages tended to increase with humidity (Table 3). This result likely stems from the following facts. In hyper-arid areas, vegetation is usually under drought stress, and has a low growth rate over a long period. For the dryland categories from hyper-arid areas to additional areas, rainfall events may increase in a sporadic way, which could lead to increases in short-term surpluses of water and thus a higher chance of creating plateau stages.

The phenomenon of linear tails in the EVI2 trajectories was limited, with a pixel proportion of 0.7 % in the greenup phase and 0.8 % in the dormancy phase over the 10-year period. The tail before the greenup phase of a vegetation community can probably be attributed to a quantity of the rainfall that is insufficient to boost plant growth or rare species variations, and could also be affected after the late senescence phase by vegetation that dries out continuously and slowly over a long

period, as in crop residuals. In most cases, the signals of tails could be removed using noise-removal algorithms to improve the quality of the VI time series, such as the background retrieval algorithm in the current HPLM (Zhang, 2015). As a result, the linear parameter in E-HPLM could give an overall minor improvement in the retrievals of the phenometrics.

The improvement in LSP retrievals from E-HPLM across the global drylands was moderate in comparison with the HPLM retrievals, with an MAD of less than five days. This is as expected, since the EVI2 trajectories in most of the pixels were regular, without the occurrences of plateaus or tails. In these cases, the results from E-HPLM and HPLM were identical. However, the advantages of E-HPLM were evident for the pixels with plateau stages, as it was able to reduce the uncertainties by 9–14 days for the four phenometrics.

E-HPLM was carefully evaluated, although more robust validation was limited by data availability. Field-based observations of one or a few plant species are barely representative of the vegetation community within a satellite pixel (Delbart et al., 2015; Ye et al., 2022). Currently, the most commonly used validation method is to compare LSP retrievals for coarse pixels (such as from MODIS or VIIRS LSP) with observations from fine resolution data (such as from Landsat or PhenoCam) (Klosterman et al., 2014; Liu et al., 2017a; Moon et al., 2021; Moon et al., 2019; Shen et al., 2021; Zhang et al., 2018a). However, the fine resolution phenometrics are themselves calculated from similar mathematical formulas, which also require validation. Hence, in this study, E-HPLM was evaluated by comparing it with HPLM in terms of retrieving phenometrics from VIIRS, PhenoCam, and HLS-PhenoCam time series. These evaluations demonstrated that compared with HPLM, E-HPLM could reduce the phenological uncertainty by as much as six days, which varied with types of land cover and dryland (Figs. 11 and 12 and Table 4–7). However, both E-HPLM and HPLM produced an overall MAD of three to four weeks based on four phenometrics across the various types of dryland. This large value for the MAD was similar to values in previous studies that compared satellite phenology retrievals and PhenoCam observations in drylands, in some cases over two months for grasslands, shrublands, and savannas (Liu et al., 2017c; Peng et al., 2017a). Indeed, the MAD found in this study for drylands was relatively large compared to the accuracy evaluations of VIIRS and MODIS

Table 7

Mean absolute difference (MAD) between VIIRS and HLS-PhenoCam phenology retrieved with either E-HPLM or HPLM in different drylands. Only pixels with either plateau stages or linear tails were used. Negative values indicate that E-HPLM produces lower MAD than HPLM. GR: grasslands, SH: shrublands, CR: croplands.

Phenometrics	Drylands	Percent (%)				MAD		
		Total	GR	SH	CR	E-HPLM	HPLM	Difference
Greenup onset	Arid areas	12.8	1.0	11.7	0.0	15.4	17.1	-1.7
	Semi-arid areas	59.1	39.0	12.6	1.9	20.7	20.5	0.2
	Dry sub-humid areas	19.9	9.4	1.2	6.2	23.2	24.9	-1.7
	Additional areas	8.3	1.4	0.0	6.7	26.9	28.9	-2.0
Maturity onset	Arid areas	9.5	1.0	8.5	0.0	34.2	38.7	-4.5
	Semi-arid areas	57.2	39.4	10.4	2.3	20.2	24.4	-4.2
	Dry sub-humid areas	18.2	10.5	1.1	5.0	19.4	20.0	-0.6
	Additional areas	15.1	5.8	0.0	5.3	13.5	18.6	-5.1
Senescence onset	Arid areas	7.9	0.6	7.3	0.0	23.2	22.8	0.4
	Semi-arid areas	64.0	45.9	9.1	2.7	17.8	19.8	-2.0
	Dry sub-humid areas	20.5	13.1	0.5	4.8	19.2	20.7	-1.5
	Additional areas	7.6	4.0	0.0	2.9	13.3	17.9	-4.6
Dormancy onset	Arid areas	9.2	0.4	8.7	0.0	13.8	17.0	-3.2
	Semi-arid areas	61.4	47.7	5.7	3.0	21.2	21.4	-0.2
	Dry sub-humid areas	21.0	11.6	0.8	6.0	17.0	18.3	-1.3
	Additional areas	8.4	4.8	0.0	3.2	12.9	13.1	-0.2

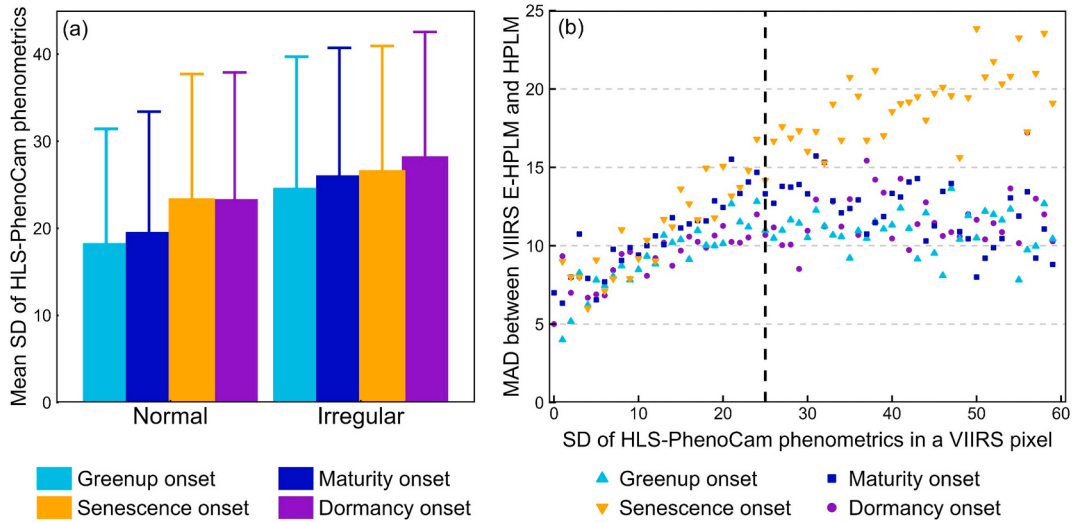


Fig. 13. Impacts of pixel heterogeneity on phenological retrievals. (a) Mean standard deviation (SD) of HLS-PhenoCam phenometrics within a VIIRS pixel under two scenarios: Normal (no plateau stages and linear tails in a VIIRS time series) and Irregular (existing plateau stages or linear tails in a VIIRS time series), where the SD value indicates the phenological heterogeneity of a VIIRS pixel. (b) Mean absolute difference (MAD) between E-HPLM and HPLM retrievals against the SD of HLS-PhenoCam phenometrics within a VIIRS pixel.

phenology reported in humid ecosystems (Liu et al., 2017b; Purdy et al., 2023; Rodriguez-Galiano et al., 2015; Ye et al., 2022; Zhang et al., 2018a). This phenomenon is likely associated with the heterogeneity of plant species within 500 m VIIRS pixels, their different sensitivity to sporadic rainfall patterns, and their resilience to drought events (Liu et al., 2024; Peng et al., 2021; Zhang et al., 2017), which significantly shape the temporal trajectories of vegetation greenness in drylands. As a result, the variation in the phenological date of the same event within a 500 m pixel was often greater than three months (Peng et al., 2021; Liu et al., 2024). Such a large spatial variation in a 500 m area was also demonstrated in deciduous forests (Fisher et al., 2006), as well as mixed and coniferous forests (Nijland et al., 2016). The E-HPLM algorithm developed in this study can handle an irregular trajectory of a VI, and can partly resolve the impacts of spatial heterogeneity (Fig. 13). However, the heterogeneity of a satellite pixel cannot be solely explained by the growth of vegetation (Fig. 13b). Due to the complexity of scaling effects (Fisher et al., 2006; Nijland et al., 2016; Zhang et al., 2017), it is very challenging to aggregate the heterogeneous PhenoCam or HLS-PhenoCam phenological dates to evaluate 500 m VIIRS phenology retrievals. Therefore, new methodologies need to be proposed to

effectively validate satellite-retrieved LSP products.

6. Conclusions

We developed an E-HPLM algorithm for the reconstruction of irregular EVI2 time series with multiple plateau stages or long linear tails during a vegetation growing season. This model was specifically designed for seasonal vegetation development in drylands, but it will also be applicable to ecosystems where the temporal vegetation greenness shows irregular patterns. Our E-HPLM approach performed much better than HPLM in fitting the PhenoCam GCC and VIIRS EVI2 time series when plateau stages or linear tails were present in the time series. E-HPLM was verified for retrieving VIIRS LSP from 2013 to 2022 in global drylands, and was able to reduce uncertainty by about 10 days in the pixels with plateau stages globally in comparison with the HPLM algorithm (VIIRS GLSP product). Compared to HPLM, E-HPLM derived a later greenup onset and an earlier dormancy onset, resulting in a shorter growing season. E-HPLM is expected to significantly improve global phenology retrievals, as plateau stages appeared in 74–78 % of dryland pixels over the 10-year period considered here, although the impacts

from long linear tails affected less than 0.8 % of pixels. When comparing VIIRS LSP with PhenoCam and HLS-PhenoCam observations for pixels with plateau stages, the results showed that the E-HPLM retrievals generally had a smaller MAD than the HPLM retrievals. These findings suggest that the proposed E-HPLM algorithm can significantly improve the reconstruction of temporal trajectories that are critical for accurately simulating greenness changes and extracting phenological dates in drylands as well as for pixels with irregular temporal patterns in other ecosystems.

CRediT authorship contribution statement

Yongchang Ye: Writing – review & editing, Writing – original draft, Validation, Methodology, Investigation, Formal analysis, Data curation. **Xiaoyang Zhang:** Writing – review & editing, Supervision, Software, Resources, Project administration, Methodology, Investigation, Funding acquisition, Formal analysis, Data curation, Conceptualization. **Jianmin Wang:** Writing – review & editing, Methodology, Investigation, Formal analysis, Data curation. **Khuong H. Tran:** Writing – review & editing, Methodology, Investigation, Formal analysis. **Yuxia Liu:** Writing – review & editing, Methodology, Investigation, Formal analysis. **Yu Shen:** Writing – review & editing, Methodology, Investigation, Formal analysis. **Shuai Gao:** Writing – review & editing, Methodology, Investigation, Formal analysis. **Shuai An:** Writing – review & editing, Methodology, Investigation, Formal analysis, Conceptualization.

Declaration of competing interest

The authors declare that they have no known competing financial interests or personal relationships that could have appeared to influence the work reported in this paper.

Acknowledgments

This work was supported by the NASA Grant 80NSSC21K1962. We would like to express our profound gratitude to LP DAAC for providing the MODIS and VIIRS satellite data, to PhenoCam for providing PhenoCam images and associated tools, and to UNEP-WCMC for providing the global dryland boundary file.

Data availability

Data will be made available on request.

References

- Ahlström, A., Raupach, M.R., Schurgers, G., Smith, B., Arneth, A., Jung, M., Reichstein, M., Canadell, J.G., Friedlingstein, P., Jain, A.K., Kato, E., Poulter, B., Sitch, S., Stocker, B.D., Vivoy, N., Wang, Y.P., Wiltshire, A., Zaehle, S., Zeng, N., 2015. The dominant role of semi-arid ecosystems in the trend and variability of the land CO₂ sink. *Science* 348, 895–899. <https://doi.org/10.1126/science.aaa1668>.
- Ammar, M.E., Davies, E.G.R., 2019. On the accuracy of crop production and water requirement calculations: process-based crop modeling at daily, semi-weekly, and weekly time steps for integrated assessments. *J. Environ. Manag.* 238, 460–472. <https://doi.org/10.1016/j.jenvman.2019.03.030>.
- Beck, P.S.A., Atzberger, C., Hogda, K.A., Johansen, B., Skidmore, A.K., 2006. Improved monitoring of vegetation dynamics at very high latitudes: a new method using MODIS NDVI. *Remote Sens. Environ.* 100, 321–334. <https://doi.org/10.1016/j.rse.2005.10.021>.
- Bolton, D.K., Gray, J.M., Melaas, E.K., Moon, M., Eklundh, L., Friedl, M.A., 2020. Continental-scale land surface phenology from harmonized Landsat 8 and Sentinel-2 imagery. *Remote Sens. Environ.* 240. <https://doi.org/10.1016/j.rse.2020.111685>.
- Cao, R.Y., Chen, J., Shen, M.G., Tang, Y.H., 2015. An improved logistic method for detecting spring vegetation phenology in grasslands from MODIS EVI time-series data. *Agric. For. Meteorol.* 200, 9–20. <https://doi.org/10.1016/j.agrformet.2014.09.009>.
- Cheng, Y., Vrielink, A., Fava, F., Meroni, M., Marshall, M., Gachoki, S., 2020. Phenology of short vegetation cycles in a Kenyan rangeland from PlanetScope and Sentinel-2. *Remote Sens. Environ.* 248. <https://doi.org/10.1016/j.rse.2020.112004>.
- Cook, G.D., Williams, R.J., Hutley, L.B., O’Grady, A.P., Liedloff, A.C., 2002. Variation in vegetative water use in the savannas of the north Australian tropical transect. *J. Veg. Sci.* 13, 413–418. <https://doi.org/10.1111/j.1654-1103.2002.tb02065.x>.
- Currier, C.M., Sala, O.E., 2022. Precipitation versus temperature as phenology controls in drylands. *Ecology* 103. <https://doi.org/10.1002/ecy.3793>.
- Delbart, N., Kergoat, L., Le Toan, T., Lhermitte, J., Picard, G., 2005. Determination of phenological dates in boreal regions using normalized difference water index. *Remote Sens. Environ.* 97, 26–38. <https://doi.org/10.1016/j.rse.2005.03.011>.
- Delbart, N., Beaubien, E., Kergoat, L., Toan, T.L., 2015. Comparing land surface phenology with leafing and flowering observations from the PlantWatch citizen network. *Remote Sens. Environ.* 160, 273–280. <https://doi.org/10.1016/j.rse.2015.01.012>.
- Dong, Y.Q., Zhou, Y., Zhang, L., Tian, F., Xie, Q.Y., Chen, Y.Y., Ruan, L.L., Zhang, B., 2025. An enhanced phenology dataset for global drylands from 2001 to 2019. *Sci Data* 12. <https://doi.org/10.1038/s41597-025-05519-2>.
- Elmore, A.J., Guinn, S.M., Minsley, B.J., Richardson, A.D., 2012. Landscape controls on the timing of spring, autumn, and growing season length in mid-Atlantic forests. *Glob. Chang. Biol.* 18, 656–674. <https://doi.org/10.1111/j.1365-2486.2011.02521.x>.
- Fisher, J.I., Mustard, J.F., Vadéboncoeur, M.A., 2006. Green leaf phenology at Landsat resolution: scaling from the field to the satellite. *Remote Sens. Environ.* 100, 265–279. <https://doi.org/10.1016/j.rse.2005.10.022>.
- Fontana, F.M.A., Trishchenko, A.P., Khlopovkin, K.V., Luo, Y., Wunderle, S., 2009. Impact of orthorectification and spatial sampling on maximum NDVI composite data in mountain regions. *Remote Sens. Environ.* 113, 2701–2712. <https://doi.org/10.1016/j.rse.2009.08.008>.
- Friedl, M., Sulla-Menashe, D., 2022. MCD12Q1 MODIS/Terra+Aqua Land Cover Type Yearly 13 Global 500m SIN Grid V061 [Data set]. NASA EOSDIS Land Processes DAAC. <https://doi.org/10.5067/MODIS/MCD12Q1.061> accessed on 13 June 2023.
- Ganguly, S., Friedl, M.A., Tan, B., Zhang, X.Y., Verma, M., 2010. Land surface phenology from MODIS: characterization of the collection 5 global land cover dynamics product. *Remote Sens. Environ.* 114, 1805–1816. <https://doi.org/10.1016/j.rse.2010.04.005>.
- Gray, J., Sulla-Menashe, D., Friedl, M.A., 2019. User Guide to Collection 6 MODIS Land Cover Dynamics (MCD12Q2) Product. https://lpdaac.usgs.gov/documents/1310/mcd12q2_v6_user_guide.pdf.
- Hargrove, W.W., Spruce, J.P., Gasser, G.E., Hoffman, F.M., 2009. Toward a National Early Warning System for Forest disturbances using remotely sensed canopy phenology. *Photogramm. Eng. Remote. Sens.* 75, 1150–1156. <https://doi.org/10.1016/j.rse.2009.08.008>.
- Hmimina, G., Dufréne, E., Pontailler, J.Y., Delpierre, N., Aubinet, M., Caquet, B., de Grandcourt, A., Burban, B., Flechard, C., Granier, A., Gross, P., Heinesch, B., Longdoz, B., Moureaux, C., Ourcival, J.M., Rambal, S., Saint André, L., Soudani, K., 2013. Evaluation of the potential of MODIS satellite data to predict vegetation phenology in different biomes: an investigation using ground-based NDVI measurements. *Remote Sens. Environ.* 132, 145–158. <https://doi.org/10.1016/j.rse.2013.01.010>.
- Hulley, G., Islam, T., Freepartner, R., Malakar, N., 2016. Visible Infrared Imaging Radiometer Suite (VIIRS) Land Surface Temperature and Emissivity Product Collection 1 Algorithm Theoretical Basis Document. https://lpdaac.usgs.gov/documents/1332/VNP21_ATBD_V1.pdf.
- Jonsson, P., Eklundh, L., 2002. Seasonality extraction by function fitting to time-series of satellite sensor data. *ITGRS* 40, 1824–1832. <https://doi.org/10.1109/Tgrs.2002.802519>.
- Kandasamy, S., Baret, F., Verger, A., Neveux, P., Weiss, M., 2013. A comparison of methods for smoothing and gap filling time series of remote sensing observations - application to MODIS LAI products. *Biogeosciences* 10, 4055–4071. <https://doi.org/10.5194/bg-10-4055-2013>.
- Klosterman, S.T., Hufkens, K., Gray, J.M., Melaas, E., Sonnentag, O., Lavine, I., Mitchell, L., Norman, R., Friedl, M.A., Richardson, A.D., 2014. Evaluating remote sensing of deciduous forest phenology at multiple spatial scales using PhenoCam imagery. *Biogeosciences* 11, 4305–4320. <https://doi.org/10.5194/bg-11-4305-2014>.
- Knapp, A.K., Chen, A.P., Griffin-Nolan, R.J., Baur, L.E., Carroll, C.J.W., Gray, J.E., Hoffman, A.M., Li, X.R., Post, A.K., Slette, I.J., Collins, S.L., Luo, Y.Q., Smith, M.D., 2020. Resolving the dust bowl paradox of grassland responses to extreme drought. *Proc. Natl. Acad. Sci. USA* 117, 22249–22255. <https://doi.org/10.1073/pnas.1922030117>.
- Kross, A., Fernandes, R., Seaquist, J., Beaubien, E., 2011. The effect of the temporal resolution of NDVI data on season onset dates and trends across Canadian broadleaf forests. *Remote Sens. Environ.* 115, 1564–1575. <https://doi.org/10.1016/j.rse.2011.02.015>.
- Lian, X., Piao, S.L., Chen, A.P., Huntingford, C., Fu, B.J., Li, L.Z.X., Huang, J.P., Sheffield, J., Berg, A.M., Keenan, T.F., McVicar, T.R., Wada, Y., Wang, X.H., Wang, T., Yang, Y.T., Roderick, M.L., 2021. Multifaceted characteristics of dryland aridity changes in a warming world. *Nat. Rev. Earth Env.* 2, 232–250. <https://doi.org/10.1038/s43017-021-001440>.
- Liu, L.L., Zhang, X.Y., Yu, Y.Y., Donnelly, A., 2017a. Detecting spatiotemporal changes of peak foliage coloration in deciduous and mixedforests across the central and eastern United States. *Environ. Res. Lett.* 12. <https://doi.org/10.1088/1748-9326/aa5b3a>.
- Liu, L.L., Zhang, X.Y., Yu, Y.Y., Guo, W., 2017b. Real-time and short-term predictions of spring phenology in North America from VIIRS data. *Remote Sens. Environ.* 194, 89–99. <https://doi.org/10.1016/j.rse.2017.03.009>.
- Liu, Y., Hill, M.J., Zhang, X.Y., Wang, Z.S., Richardson, A.D., Hufkens, K., Filippa, G., Baldocchi, D.D., Ma, S.Y., Verfaillie, J., Schaaf, C.B., 2017c. Using data from Landsat, MODIS, VIIRS and PhenoCams to monitor the phenology of California oak/grass savanna and open grassland across spatial scales. *Agric. For. Meteorol.* 237, 311–325. <https://doi.org/10.1016/j.agrformet.2017.02.026>.

- Liu, H.H., Liu, Y., Chen, Y., Fan, M.E., Chen, Y., Gang, C.C., You, Y.F., Wang, Z.A., 2023. Dynamics of global dryland vegetation were more sensitive to soil moisture: evidence from multiple vegetation indices. *Agric. For. Meteorol.* 331. <https://doi.org/10.1016/j.agrformet.2023.109327>.
- Liu, Y.X., Zhang, X.Y., Shen, Y., Ye, Y.C., Gao, S., Tran, K.H., 2024. Evaluation of PlanetScope-detected plant-specific phenology using infrared-enabled PhenoCam observations in semi-arid ecosystems. *Isprs J. Photogramm.* 210, 242–259. <https://doi.org/10.1016/j.isprsjprs.2024.03.017>.
- Ma, X.L., Huete, A., Yu, Q., Coupe, N.R., Davies, K., Broich, M., Ratana, P., Beringer, J., Hutley, L.B., Cleverly, J., Boulain, N., Eamus, D., 2013. Spatial patterns and temporal dynamics in savanna vegetation phenology across the north Australian tropical transect. *Remote Sens. Environ.* 139, 97–115. <https://doi.org/10.1016/j.rse.2013.07.030>.
- Middleton, N.J., Sternberg, T., 2013. Climate hazards in drylands: a review. *Earth Sci. Rev.* 126, 48–57. <https://doi.org/10.1016/j.earscirev.2013.07.008>.
- Millennium Ecosystem Assessment, 2005. Millennium Ecosystem Assessment: MA Ecosystems. In: In Palisades. NASA Socioeconomic Data and Applications Center (SEDAC), New York. <https://doi.org/10.7927/H4KW5CZ6>.
- Miura, T., Huete, A.R., Yoshioka, H., 2000. Evaluation of sensor calibration uncertainties on vegetation indices for MODIS. *ITGRS* 38, 1399–1409. <https://doi.org/10.1109/36.843034>.
- Moody, A., Johnson, D.M., 2001. Land-surface phenologies from AVHRR using the discrete Fourier transform. *Remote Sens. Environ.* 75, 305–323. [https://doi.org/10.1016/S0034-4257\(00\)00175-9](https://doi.org/10.1016/S0034-4257(00)00175-9).
- Moon, M., Zhang, X.Y., Henebry, G.M., Liu, L.L., Gray, J.M., Melaas, E.K., Friedl, M.A., 2019. Long-term continuity in land surface phenology measurements: a comparative assessment of the MODIS land cover dynamics and VIIRS land surface phenology products. *Remote Sens. Environ.* 226, 74–92. <https://doi.org/10.1016/j.rse.2019.03.034>.
- Moon, M., Richardson, A.D., Friedl, M.A., 2021. Multiscale assessment of land surface phenology from harmonized Landsat 8 and Sentinel-2, PlanetScope, and PhenoCam imagery. *Remote Sens. Environ.* 266. <https://doi.org/10.1016/j.rse.2021.112716>.
- Moon, M., Richardson, A.D., Milliman, T., Friedl, M.A., 2022. A high spatial resolution land surface phenology dataset for AmeriFlux and NEON sites. *Sci Data* 9. <https://doi.org/10.1038/s41597-022-01570-5>.
- Muthoka, J.M., Antonarakis, A.S., Vrielin, A., Fava, F., Salakpi, E.E., Rowhani, P., 2022. Assessing drivers of intra-seasonal grassland dynamics in a Kenyan savannah using digital repeat photography. *Ecol. Indic.* 142. <https://doi.org/10.1016/j.ecolind.2022.109223>.
- Nijland, W., Bolton, D.K., Coops, N.C., Stenhouse, G., 2016. Imaging phenology; scaling from camera plots to landscapes. *Remote Sens. Environ.* 177, 13–20. <https://doi.org/10.1016/j.rse.2016.02.018>.
- Pastick, N.J., Wylie, B.K., Wu, Z.T., 2018. Spatiotemporal analysis of Landsat-8 and Sentinel-2 data to support monitoring of dryland ecosystems. *Remote Sens. Environ.* 200. <https://doi.org/10.10339/rs10050791>.
- Peng, D.L., Wu, C.Y., Li, C.J., Zhang, X.Y., Liu, Z.J., Ye, H.C., Luo, S.Z., Liu, X.J., Hug, Y., Fang, B., 2017a. Spring green-up phenology products derived from MODIS NDVI and EVI: Intercomparison, interpretation and validation using National Phenology Network and AmeriFlux observations. *Ecol. Indic.* 77, 323–336. <https://doi.org/10.1016/j.ecolind.2017.02.024>.
- Peng, D.L., Zhang, X.Y., Wu, C.Y., Huang, W.J., Gonsamo, A., Huete, A.R., Didan, K., Tan, B., Liu, X.J., Zhang, B., 2017b. Intercomparison and evaluation of spring phenology products using National Phenology Network and AmeriFlux observations in the contiguous United States. *Agric. For. Meteorol.* 242, 33–46. <https://doi.org/10.1016/j.agrformet.2017.04.009>.
- Peng, D.L., Wang, Y., Xian, G., Huete, A.R., Huang, W.J., Shen, M.G., Wang, F.M., Yu, L., Liu, L.Y., Xie, Q.Y., Liu, L.L., Zhang, X.Y., 2021. Investigation of land surface phenology detections in shrublands using multiple scale satellite data. *Remote Sens. Environ.* 252. <https://doi.org/10.1016/j.rse.2020.112133>.
- Piao, S.L., Fang, J.Y., Zhou, L.M., Ciais, P., Zhu, B., 2006. Variations in satellite-derived phenology in China's temperate vegetation. *Glob. Chang. Biol.* 12, 672–685. <https://doi.org/10.1111/j.1365-2486.2006.01123.x>.
- Pouliot, D., Latifovic, R., Fernandes, R., Olthof, I., 2011. Evaluation of compositing period and AVHRR and MERIS combination for improvement of spring phenology detection in deciduous forests. *Remote Sens. Environ.* 115, 158–166. <https://doi.org/10.1016/j.rse.2010.08.014>.
- Purdy, L.M., Sang, Z.H.H., Beaubien, E., Hamann, A., 2023. Validating remotely sensed land surface phenology with leaf out records from a citizen science network. *IJAEO* 116. <https://doi.org/10.1016/j.jag.2022.103148>.
- Reeves, M.C., Winslow, J.C., Running, S.W., 2001. Mapping weekly rangeland vegetation productivity using MODIS algorithms. *J. Range Manag.* 54, A90.
- Richardson, A.D., Keenan, T.F., Migliavacca, M., Ryu, Y., Sonnentag, O., Toomey, M., 2013. Climate change, phenology, and phenological control of vegetation feedbacks to the climate system. *Agric. For. Meteorol.* 169, 156–173. <https://doi.org/10.1016/j.agrformet.2012.09.012>.
- Richardson, A.D., Hufkens, K., Milliman, T., Aubrecht, D.M., Chen, M., Gray, J.M., Johnston, M.R., Keenan, T.F., Klosterman, S.T., Kosmala, M., Melaas, E.K., Friedl, M.A., Frolking, S., 2018. Tracking vegetation phenology across diverse north American biomes using PhenoCam imagery. *Sci Data* 5. <https://doi.org/10.1038/sdata.2018.28>.
- Rodriguez-Galiano, V.F., Dash, J., Atkinson, P.M., 2015. Intercomparison of satellite sensor land surface phenology and ground phenology in Europe. *Geophys. Res. Lett.* 42, 2253–2260. <https://doi.org/10.1002/2015gl063586>.
- Roman, M.O., Justice, C., Paynter, I., Boucher, P.B., Devadiga, S., Endsley, A., Erb, A., Friedl, M., Gao, H.L., Giglio, L., Gray, J.M., Hall, D., Hulley, G., Kimball, J., Knyazikhin, Y., Lyapustin, A., Myneni, R.B., Noojipady, P., Pu, J.B., Riggs, G.,
- Sarkar, S., Schaaf, C., Shah, D.P., Tran, K.H., Vermote, E., Wang, D.D., Wang, Z.S., Wu, A.S., Ye, Y.C., Shen, Y., Zhang, S., Zhang, X.Y., Zhao, M.S., Davidson, C., Wolfe, R., 2024. Continuity between NASA MODIS collection 6.1 and VIIRS collection 2 land products. *Remote Sens. Environ.* 302. <https://doi.org/10.1016/j.rse.2023.113963>.
- Schaaf, C., Wang, Z., Zhang, X., Strahler, A., 2018. VIIRS/NPP BRDF/Albedo Nadir BRDF-Adjusted Ref Daily L3 Global 500m SIN Grid V001 [Data set]. NASA EOSDIS Land Processes DAAC. <https://doi.org/10.5067/VIIRS/VNP43IA4.001> accessed on 13 June 2023.
- Shen, M.G., Piao, S.L., Cong, N., Zhang, G.X., Janssens, I.A., 2015. Precipitation impacts on vegetation spring phenology on the Tibetan plateau. *Glob. Chang. Biol.* 21, 3647–3656. <https://doi.org/10.1111/gcb.12961>.
- Shen, Y., Zhang, X.Y., Wang, W.L., Nemani, R., Ye, Y.C., Wang, J.M., 2021. Fusing geostationary satellite observations with harmonized Landsat-8 and Sentinel-2 time series for monitoring field-scale land surface phenology. *Remote Sens.* 13. <https://doi.org/10.3390/rs13214465>.
- Skakun, S., Justice, C.O., Vermote, E., Roger, J.C., 2018. Transitioning from MODIS to VIIRS: an analysis of inter-consistency of NDVI data sets for agricultural monitoring. *Int. J. Remote Sens.* 39, 971–992. <https://doi.org/10.1080/01431161.2017.1395970>.
- Smith, W.K., Dannenberg, M.P., Yan, D., Herrmann, S., Barnes, M.L., Barron-Gafford, G.A., Biederman, J.A., Ferrenberg, S., Fox, A.M., Hudson, A., Knowles, J.F., MacBean, N., Moore, D.J.P., Nagler, P.L., Reed, S.C., Rutherford, W.A., Scott, R.L., Wang, X., Yang, J.L., 2019. Remote sensing of dryland ecosystem structure and function: progress, challenges, and opportunities. *Remote Sens. Environ.* 233. <https://doi.org/10.1016/j.rse.2019.111401>.
- Sorensen, L., 2007. A Spatial Analysis Approach to the Global Delineation of Dryland Areas of Relevance to the CBD Programme of Work on Dry and Sub-Humid Lands. UNEP-WCMC, Cambridge, UK.
- Sulla-Menashe, D., Gray, J.M., Abercrombie, S.P., Friedl, M.A., 2019. Hierarchical mapping of annual global land cover 2001 to present: the MODIS collection 6 land cover product. *Remote Sens. Environ.* 222, 183–194. <https://doi.org/10.1016/j.rse.2018.12.013>.
- Tian, F., Cai, Z.Z., Jin, H.X., Hufkens, K., Scheifinger, H., Tagesson, T., Smets, B., Van Hoolst, R., Bonte, K., Ivits, E., Tong, X.Y., Ardö, J., Eklundh, L., 2021a. Calibrating vegetation phenology from Sentinel-2 using eddy covariance, PhenoCam, and PEP725 networks across Europe. *Remote Sens. Environ.* 260. <https://doi.org/10.1016/j.rse.2021.112456>.
- Tian, J.Q., Zhu, X.L., Chen, J., Wang, C., Shen, M.G., Yang, W., Tan, X.Y., Xu, S., Li, Z.L., 2021b. Improving the accuracy of spring phenology detection by optimally smoothing satellite vegetation index time series based on local cloud frequency. *Isprs J. Photogramm.* 180, 29–44. <https://doi.org/10.1016/j.isprsjprs.2021.08.003>.
- Tran, K.H., Zhang, X., Ye, Y., Shen, Y., Gao, S., Liu, Y., Richardson, A., 2023. HP-LSP: a reference of land surface phenology from fused harmonized Landsat and Sentinel-2 with PhenoCam data. *Sci Data* 10, 691. <https://doi.org/10.1038/s41597-023-02605-1>.
- Ukkola, A.M., De Kauwe, M.G., Roderick, M.L., Burrell, A., Lehmann, P., Pitman, A.J., 2021. Annual precipitation explains variability in dryland vegetation greenness globally but not locally. *Glob. Chang. Biol.* 27, 4367–4380. <https://doi.org/10.1111/gcb.15729>.
- UNCDD, 1994. United Nations Convention to Combat Desertification in those Countries Experiencing Serious Drought and/or Desertification.
- UNCDD, 2017. DRYLANDS. In: Johnson, Ian, Alexander, S. (Eds.), *The Global Land Outlook*, first edition, pp. 246–269. Bonn, Germany.
- UNEP/CBD/SBSTTA/5/9, 1999. Biological Diversity of Dryland, Mediterranean, Arid, Semiarid, Grassland and Savannah Ecosystems: Options for the Development of a Programme of Work. Montreal, Canada.
- Verma, M., Friedl, M.A., Finzi, A.C., Phillips, N., 2016. Multi-criteria evaluation of the suitability of growth functions for modeling remotely sensed phenology. *Ecol. Model.* 323, 123–132. <https://doi.org/10.1016/j.ecolmodel.2015.12.005>.
- Walther, S., Duveiller, G., Jung, M., Guanter, L., Cescatti, A., Camps-Valls, G., 2019. Satellite observations of the contrasting response of trees and grasses to variations in water availability. *Geophys. Res. Lett.* 46, 1429–1440. <https://doi.org/10.1029/2018gl080535>.
- Wang, C., Beringer, J., Hutley, L.B., Cleverly, J., Li, J., Liu, Q.H., Sun, Y., 2019. Phenology dynamics of dryland ecosystems along the north Australian tropical transect revealed by satellite solar-induced chlorophyll fluorescence. *Geophys. Res. Lett.* 46, 5294–5302. <https://doi.org/10.1029/2019gl082716>.
- Wang, H., Liu, Y.X., Wang, Y.J., Yao, Y., Wang, C.X., 2023. Land cover change in global drylands: a review. *Sci. Total Environ.* 863. <https://doi.org/10.1016/j.scitotenv.2022.160943>.
- Wu, C.Y., Hou, X.H., Peng, D.L., Gonsamo, A., Xu, S.G., 2016. Land surface phenology of China's temperate ecosystems over 1999–2013: spatial-temporal patterns, interaction effects, covariation with climate and implications for productivity. *Agric. For. Meteorol.* 216, 177–187. <https://doi.org/10.1016/j.agrformet.2015.10.015>.
- Xie, Y.H., Lark, T.J., 2021. Mapping annual irrigation from Landsat imagery and environmental variables across the conterminous United States. *Remote Sens. Environ.* 260. <https://doi.org/10.1016/j.rse.2021.112445>.
- Xie, Y.Y., Wilson, A.M., 2020. Change point estimation of deciduous forest land surface phenology. *Remote Sens. Environ.* 240. <https://doi.org/10.1016/j.rse.2020.111698>.
- Xie, Q.Y., Cleverly, J., Moore, C.E., Ding, Y.L., Hall, C.C., Ma, X.L., Brown, L.A., Wang, C., Beringer, J., Prober, S.M., Macfarlane, C., Meyer, W.S., Yin, G.F., Huete, A., 2022. Land surface phenology retrievals for arid and semi-arid ecosystems. *Isprs J. Photogramm.* 185, 129–145. <https://doi.org/10.1016/j.isprsjprs.2022.01.017>.
- Ye, Y.C., Zhang, X.Y., Shen, Y., Wang, J.M., Crimmins, T., Scheifinger, H., 2022. An optimal method for validating satellite-derived land surface phenology using in-situ

- observations from national phenology networks. *Isprs J. Photogramm.* 194, 74–90. <https://doi.org/10.1016/j.isprsjprs.2022.09.018>.
- Zhang, X.Y., 2015. Reconstruction of a complete global time series of daily vegetation index trajectory from long-term AVHRR data. *Remote Sens. Environ.* 156, 457–472. <https://doi.org/10.1016/j.rse.2014.10.012>.
- Zhang, X.Y., 2018. Land surface phenology: Climate data record and real-time monitoring. In: Liang, S. (Ed.), *Comprehensive Remote Sensing*. Elsevier, pp. 35–52. <https://doi.org/10.1016/b978-0-12-409548-9.10351-3>.
- Zhang, X., 2024. VIIRS/NPP Land Surface Phenology Yearly L3 Global 500m SIN Grid V002 [Data set]. NASA Land Processes Distributed Active Archive Center. <https://doi.org/10.5067/VIIRS/VNP22Q2.002>. Data Accessed 19 August 2025.
- Zhang, X.Y., Friedl, M.A., Schaaf, C.B., Strahler, A.H., Hodges, J.C.F., Gao, F., Reed, B.C., Huete, A., 2003. Monitoring vegetation phenology using MODIS. *Remote Sens. Environ.* 84, 471–475. [https://doi.org/10.1016/S0034-4257\(02\)00135-9](https://doi.org/10.1016/S0034-4257(02)00135-9).
- Zhang, X.Y., Friedl, M.A., Schaaf, C.B., Strahler, A.H., 2004. Climate controls on vegetation phenological patterns in northern mid- and high latitudes inferred from MODIS data. *Glob. Chang. Biol.* 10, 1133–1145. <https://doi.org/10.1111/j.1529-8817.2003.00784.x>.
- Zhang, X.Y., Friedl, M.A., Schaaf, C.B., Strahler, A.H., Liu, Z., 2005. Monitoring the response of vegetation phenology to precipitation in Africa by coupling MODIS and TRMM instruments. *J. Geophys. Res. Atmos.* 110. <https://doi.org/10.1029/2004jd005263>.
- Zhang, X., Friedl, M., Schaaf, C., 2009. Sensitivity of vegetation phenology detection to the temporal resolution of satellite data. *Int. J. Remote Sens.* 30, 2061–2074. <https://doi.org/10.1080/01431160802549237>.
- Zhang, Y., Xiao, X.M., Zhou, S., Ciais, P., McCarthy, H., Luo, Y.Q., 2016. Canopy and physiological controls of GPP during drought and heat wave. *Geophys. Res. Lett.* 43, 3325–3333. <https://doi.org/10.1002/2016gl068501>.
- Zhang, X.Y., Wang, J.M., Gao, F., Liu, Y., Schaaf, C., Friedl, M., Yu, Y.Y., Jayavelu, S., Gray, J., Liu, L.L., Yan, D., Henebry, G.M., 2017. Exploration of scaling effects on coarse resolution land surface phenology. *Remote Sens. Environ.* 190, 318–330. <https://doi.org/10.1016/j.rse.2017.01.001>.
- Zhang, X.Y., Jayavelu, S., Liu, L.L., Friedl, M.A., Henebry, G.M., Liu, Y., Schaaf, C.B., Richardson, A.D., Gray, J., 2018a. Evaluation of land surface phenology from VIIRS data using time series of PhenoCam imagery. *Agric. For. Meteorol.* 256–257, 137–149. <https://doi.org/10.1016/j.agrformet.2018.03.003>.
- Zhang, X.Y., Liu, L.L., Liu, Y., Jayavelu, S., Wang, J.M., Moon, M., Henebry, G.M., Friedl, M.A., Schaaf, C.B., 2018b. Generation and evaluation of the VIIRS land surface phenology product. *Remote Sens. Environ.* 216, 212–229. <https://doi.org/10.1016/j.rse.2018.06.047>.
- Zhang, X.Y., Wang, J.M., Henebry, G.M., Gao, F., 2020. Development and evaluation of a new algorithm for detecting 30 m land surface phenology from VIIRS and HLS time series. *Isprs J. Photogramm.* 161, 37–51. <https://doi.org/10.1016/j.isprsjprs.2020.01.012>.
- Zhang, Y., Gentine, P., Luo, X.Z., Lian, X., Liu, Y.L., Zhou, S., Michalak, A.M., Sun, W., Fisher, J.B., Piao, S.L., Keenan, T.F., 2022. Increasing sensitivity of dryland vegetation greenness to precipitation due to rising atmospheric CO₂. *Nat. Commun.* 13. <https://doi.org/10.1038/s41467-022-32631-3>.
- Zhang, X., Henebry, G.M., Friedl, M.A., Schaaf, C., Ye, Y., Tran, K., Liu, L., 2024. Algorithm Technical Basis Document VIIRS Land Surface Phenology Product (Collection 2.0). https://viirsland.gsfc.nasa.gov/PDF/VIIRS_GLSP-ATBD_V2.pdf.